A&A 596, A11 (2016)
DOI: 10.1051/0004-6361/201629221

Astronomy & Astrophysics

Quenching of the star formation activity in cluster galaxies

A. Boselli[1,⋆], Y. Roehlly[1], M. Fossati[2,3], V. Buat[1], S. Boissier[1], M. Boquien[4], D. Burgarella[1], L. Ciesla[5], G. Gavazzi[6], and P. Serra[7]

[1] Aix-Marseille Université, CNRS, LAM, Laboratoire d'Astrophysique de Marseille, 13388 Marseille, France
e-mail: alessandro.boselli@lam.fr
[2] Universitäts-Sternwarte München, Scheinerstrasse 1, 81679 München, Germany
[3] Max-Planck-Institut für Extraterrestrische Physik, Giessenbachstrasse, 85748 Garching, Germany
[4] Unidad de Astronomia, Universidad de Antofagasta, Antofagasta, Chile
[5] Laboratoire AIM-Paris-Saclay, CEA/DSM/Irfu – CNRS – Université Paris Diderot, CEA-Saclay, 91191 Gif-sur-Yvette, France
[6] Universitá di Milano-Bicocca, piazza della scienza 3, 20100 Milano, Italy
[7] CSIRO Astronomy and Space Science, Australia Telescope National Facility, PO Box 76, Epping, NSW 1710, Australia

Received 30 June 2016 / Accepted 2 September 2016

ABSTRACT

We study the star formation quenching mechanism in cluster galaxies by fitting the spectral energy distribution (SED) of the *Herschel* Reference Survey, a complete volume-limited K-band-selected sample of nearby galaxies including objects in different density regions, from the core of the Virgo cluster to the general field. The SEDs of the target galaxies were fitted using the CIGALE SED modelling code. The truncated activity of cluster galaxies was parametrised using a specific star formation history with two free parameters, the quenching age QA and the quenching factor QF. These two parameters are crucial for the identification of the quenching mechanism, which acts on long timescales when starvation processes are at work, but is rapid and efficient when ram pressure occurs. To be sensitive to an abrupt and recent variation of the star formation activity, we combined twenty photometric bands in the UV to far-infrared in a new way with three age-sensitive Balmer line absorption indices extracted from available medium-resolution ($R \sim 1000$) integrated spectroscopy and with Hα narrow-band imaging data. The use of a truncated star formation history significantly increases the quality of the fit in HI-deficient galaxies of the sample, that is to say, in those objects whose atomic gas content has been removed during the interaction with the hostile cluster environment. The typical quenching age of the perturbed late-type galaxies is $QA \lesssim 300$ Myr whenever the activity of star formation is reduced by $50\% < QF \leq 80\%$ and $QA \lesssim 500$ Myr for $QF > 80\%$, while that of the quiescent early-type objects is $QA \simeq 1$–3 Gyr. The fraction of late-type galaxies with a star formation activity reduced by $QF > 80\%$ and with an HI-deficiency parameter $HI - def > 0.4$ drops by a factor of ∼5 from the inner half virial radius of the Virgo cluster ($R/R_{\rm vir} < 0.5$), where the hot diffuse X-ray emitting gas of the cluster is located, to the outer regions ($R/R_{\rm vir} > 4$). The efficient quenching of the star formation activity observed in Virgo suggests that the dominant stripping process is ram pressure. We discuss the implication of this result in the cosmological context of galaxy evolution.

Key words. galaxies: clusters: general – galaxies: clusters: individual: Virgo – galaxies: evolution – galaxies: interactions – galaxies: ISM – galaxies: star formation

1. Introduction

The environment plays a main role in shaping galaxy evolution. Since the seminal work of Dressler (1980), it became evident that galaxies in rich environments are systematically different from those located in the field. Dense environments are dominated by early-type galaxies and low-density regions by spirals and irregulars (e.g. Dressler 1980; Whitmore et al. 1993; Dressler et al. 1997). It has also been shown that massive local clusters are currently accreting gas-rich, star-forming systems (e.g. Tully & Shaya 1984; Colless & Dunn 1996) whose physical properties systematically change once they reach the densest regions. It is now widely recognised that late-type galaxies located in rich clusters are generally HI-deficient (Haynes et al. 1984; Gavazzi 1987; Cayatte et al. 1990; Solanes et al. 2001; Gavazzi et al. 2005, 2006a). There is growing evidence indicating that they also lack molecular gas (Fumagalli et al. 2009; Boselli et al. 2014b) and dust (Cortese et al. 2012a) with respect to similar objects in the field. The angular resolution of the HI, CO, and far-infrared images now available thanks to interferometric observations in the radio domain and to the superior quality of the instruments on board of *Herschel* revealed that cluster galaxies have truncated gaseous and dust discs (Fumagalli et al. 2009; Boselli et al. 2014b; Cortese et al. 2012a; Davis et al. 2013), suggesting that the mechanism responsible for their stripping acts outside-in. The star formation activity of the late-type galaxies in clusters is also systematically reduced with respect to that of field objects (Kennicutt 1983; Gavazzi et al. 1998, 2002a, 2006b) and is limited to the inner disc (Koopmann & Kenney 2004; Boselli & Gavazzi 2006; Cortese et al. 2012b; Fossati et al. 2013). The correlation between the molecular gas content and the activity of star formation (e.g. Bigiel et al. 2008), generally called Schmidt law (Schmidt 1959; Kennicutt 1998a), can easily explain the observed truncation of the star-forming discs of these perturbed objects.

Different mechanisms have been proposed in the literature to explain the transformation of galaxies in rich environments and the formation of the red sequence (e.g. Boselli & Gavazzi 2006, 2014). They include the gravitational interaction between

⋆ Visiting astronomer at CSIRO Astronomy and Space Science, Australia Telescope National Facility, PO Box 76, Epping, NSW 1710, Australia.

galaxies (Merritt 1983) or that with the potential well of the cluster as a whole (Byrd & Valtonen 1990), or their combined effect, which is generally called "galaxy harassment" (Moore et al. 1998). Other possible mechanisms are those related to the interaction of the galaxy interstellar medium with the hot ($T \sim 10^7$–10^8 K) and dense ($\rho_{\rm ICM} \sim 10^{-3}$ cm^{-3}) diffuse gas trapped within the potential well of the clusters observable in X-rays (Sarazin et al. 1986). These include ram pressure (Gunn & Gott 1972) and viscous stripping (Nulsen 1982) exerted by the intracluster medium (ICM) on galaxies moving at high velocity ($\sim$1000 km s^{-1}) within the cluster, or the thermal heating of the galaxy interstellar medium (ISM) once it is in contact with the hot X-ray emitting gas of the cluster (Cowie & Songaila 1977). Since a large number of cluster galaxies is accreted through small groups, the perturbing mechanisms can start to shape galaxy evolution well before the galaxy is within the massive cluster (pre-processing, e.g. Dressler 2004). Finally, it is possible that under some circumstances the ICM only perturbs the hot gas in the galaxy halo without affecting the cold component on the disc. The cold component, however, which is not replenished by fresh infalling material, is later exhausted by the star formation activity of the galaxy itself (starvation; Larson et al. 1980).

The identification of the perturbing mechanism that is responsible for quenching the star formation activity of galaxies in high-density regions is becoming one of the main challenges of modern extragalactic astronomy. The identification of the dominant perturbing mechanism, which is expected to change with the mass of galaxies and with the properties of the overdensity region, is crucial for cosmological simulations and semi-analytical models of galaxy evolution. Different mechanisms may have different effects on the morphology and internal dynamics of the stellar component, making discs thicker and increasing the bulge-to-disc ratio (gravitational perturbations), while others are expected to decrease the surface brightness of the perturbed disc (starvation). At present, models and simulations often overestimate the fraction of quiescent galaxies along the red sequence (Kang & van den Bosch 2008; Font et al. 2008; Kimm et al. 2009; Fontanot et al. 2009; Guo et al. 2011; Weinmann et al. 2011; Wang et al. 2012; Hirschmann et al. 2014; see however Henriques et al. 2015), suggesting that the physical prescriptions used to reproduce the environmental quenching are still poorly understood. An accurate identification of the dominant mechanism is also crucial for the physical understanding of the stripping process, for the calibration of tuned hydrodynamic simulations, and for the characterisation of the effects that the mechanism has on perturbed galaxies and on the stripped material.

It is critical for constraining the perturbing mechanism to identify its action radius within high-density regions with observations and to quantify the timescale necessary to significantly remove the gas and affect the star formation process (efficiency). The analysis of nearby and high-redshift clusters still gives discordant results. The detailed study of representative objects in nearby clusters such as Virgo and Coma based on dynamical modelling of their HI and CO gas kinematics (e.g. Vollmer et al. 2004), of the radial variation of their star formation properties derived from integral field unit (IFU) optical spectroscopy (e.g. Crowl & Kenney 2008), or by the comparison of multifrequency data with tuned chemo-spectrophotometric models of galaxy evolution (e.g. Boselli et al. 2006) indicate a recent and rapid truncation of their star formation activity that is consistent with a ram pressure stripping scenario. The analysis of large statistical samples of galaxies extracted from several surveys such as the SDSS, GAMA, or GALEX, or targeted observations of nearby clusters and groups combined with the results of cosmological simulations or semi-analytical models of galaxy evolution instead suggest a slow and long quenching process typical of starvation (McGee et al. 2009; Wolf et al. 2009; von der Linden et al. 2010; De Lucia et al. 2012; Wheeler et al. 2014; Taranu et al. 2014; Haines et al. 2015; Paccagnella et al. 2016). Other works suggest a bimodal evolution, with an inefficient quenching at early epochs, when galaxies become satellites of more massive halos, and then a rapid quenching when these still relative small systems are accreted in massive clusters (pre-processing; e.g. Wetzel et al. 2012, 2013; Muzzin et al. 2012; Wijesinghe et al. 2012).

The identification of the perturbing mechanism requires an accurate reconstruction of the star formation history of galaxies in different environments. This is generally done using photometric and spectroscopic data to characterise the stellar emission in the UV to near-infrared spectral domain. The typical colours of galaxies in these bands are sensitive to their underlying stellar populations, and become redder whenever the star formation activity decreases because it is perturbed by the surrounding environment. The reconstruction of the star formation history of perturbed galaxies using these sets of data, however, is limited by the fact that other physical mechanisms such as dust attenuation and metallicity might affect the colours of galaxies in a similar way. To overcome this problem and limit any possible degeneracy between the effects of dust attenuation and ageing of the stellar populations, astronomers developed spectral energy distribution (SED) fitting codes in the UV to far-infrared. These codes, by measuring the total energy emitted by dust in the far-infrared, are able to quantify the dust attenuation on the stellar emission in a self-consistent way and are therefore now widely used to study the star formation history of different samples of galaxies (e.g. GRASIL: Silva et al. 1998; MAGPHYS: da Cunha et al. 2008).

In the past years a huge number of multifrequency data, from the UV to the radio centimetre, have been gathered for a complete volume-limited sample of nearby galaxies, the *Herschel* Reference Survey (HRS). This sample includes galaxies in different density regions, from the core of the Virgo cluster to the general field, and is therefore perfectly suited for environmental studies (Boselli et al. 2010a). These data are perfectly suited to be fitted with CIGALE, a modelling code designed to reconstruct the star formation history of galaxies through an analysis of their UV to far-infrared SED (Noll et al. 2009). In this work we improve this SED fitting code to combine in an original manner twenty photometric bands of imaging data with three age-sensitive spectroscopic indices (Balmer absorption lines) derived from integrated spectroscopy (Boselli et al. 2013) and narrow-band Hα imaging data (Boselli et al. 2015) with the aim of characterising the quenching star formation episode. We previously explored the use of the SED fitting analysis to reproduce the variations on the star formation history of cluster galaxies using only broad-band imaging photometry in Ciesla et al. (2016). The present work is thus a further developement of this technique. To date, the combination of photometric and spectroscopic data in the SED fitting analysis has been limited to the stellar plus nebular emission (Pacifici et al. 2012, 2015; Newman et al. 2014; Thomas et al. 2016; Chevallard & Charlot 2016; Lopez Fernandez et al. 2016). Our work is the first to extend this technique to a much wider spectral domain, from the UV to the far-infrared, where the far-infrared emission is used through an energy balance to break any possible degeneracy that might be due to dust attenuation in the observed stellar emission. The paper is structured as follows: we describe the sample in Sect. 2,

Table 1. Morphological distribution of the HRS.

Type	HRS	Analysed galaxies[a]
E	19	6
S0	36	15
S0a	4	1
Sa	27	13
Sab	22	7
Sb	52	39
Sbc	33	19
Sc	39	28
Scd	30	26
Sd	19	13
Sm-Im-BCD	39	23

Notes. [(a)] The galaxies analysed in this work have photometric data in all the following bands: *FUV* and *NUV* from GALEX, *gri* from SDSS, *JHK* from 2MASS, 11 and 22 μm from WISE, 100 and 160 μm from PACS and 250, 350, 500 μm from SPIRE, as well as Hα imaging data and Balmer absorption lines from integrated spectroscopy.

the multifrequency data in Sect. 3, and the SED fitting technique and procedure in Sect. 4. Section 4 also includes several tests done on mock samples to check the reliability of the output parameters. In Sect. 5 we apply the SED fitting code to a dozen representative galaxies for which independent results are available in the literature, and in Sect. 6 we expand this to the whole HRS sample. We analyse this in Sect. 7 and discuss it in Sect. 8. In Appendix A we discuss the effects of adopting different star formation histories on the derived quenching parameters. For a fair comparison with models and simulations, we recall that the typical distance of the main body of the Virgo cluster is 17 Mpc (Gavazzi et al. 1999; Mei et al. 2007) and its total dynamical mass M_{200} $(1.4-4.2) \times 10^{14}$ $M_{\odot}$ (McLaughlin 1999; Urban et al. 2011; Nulsen & Bohringer 1995; Schindler et al. 1999).

2. Sample

The sample analysed in this work has been extracted from the HRS (Boselli et al. 2010a). The HRS is a volume-limited ($15 \leq D \leq 25$ Mpc) K-band-selected (2MASS $K \leq 12$ mag for late-type galaxies, $K \leq 8.7$ mag for early-type ellipticals and lenticulars) complete sample of 322 nearby galaxies. As selected, the sample spans a wide range in morphological type (E, S0, spirals, BCDs, and Im, see Table 1) and stellar mass ($10^8 \leq M_{\rm star} \leq 10^{11}$ $M_{\odot}$), making the HRS a statistically representative stellar mass selected sample of the nearby Universe (Boselli et al. 2010a). The spectrophotometric data required for this analysis are available for 168/260 late-type galaxies of the sample, but only for 22/62 early-type galaxies (6/19 E, 15/36 S0, 1/4 S0a). We exclude form the following analysis the radio galaxies M 87 (Virgo A) and M 84 because their far-infrared emission is due to synchrotron radiation (Baes et al. 2010; Boselli et al. 2010b, 2012). The sample is ideally suited for environmental studies because it includes galaxies in a wide range of densities, from the dense core of the Virgo cluster to small groups, binary systems, and relatively isolated objects in the field. Strong observational evidence has been collected so far that indicates that the HRS galaxies in the Virgo cluster have been perturbed by their interaction with the hostile environment (Cortese et al. 2010, 2011, 2012a,b, 2016; Boselli et al. 2014b, 2015). Although a few galaxies show nuclear activity (Gavazzi et al., in prep.), the contribution of the AGN to the integrated spectrum is negligible (Boselli et al. 2013). The HRS is also ideally defined because it includes a large number of well-studied Virgo cluster galaxies in which the comparison of their kinematic and spectrophotometric properties were crucial to identify the perturbing process and dating the epoch of the first interaction with the hostile environment (Vollmer et al. 1999, 2000, 2004, 2005, 2006, 2008a,b, 2009, 2012; Vollmer 2003; Kenney et al. 2004; Boselli et al. 2005, 2006; Crowl & Kenney 2008; Abramson et al. 2011; Kenney et al. 2014; Abramson & Kenney 2014; Cortes et al. 2015).

3. Data

The HRS is perfectly suited for an SED analysis because photometric and spectroscopic data covering the whole electromagnetic spectrum are available for all galaxies. All photometric and spectroscopic data are integrated quantities and therefore do not deserve any aperture correction, which is a probable source of systematic effects in perturbed galaxies given the outside-in truncation of the star-forming disc. The objects analysed in this work have been detected in all the following photometric bands: *FUV* and *NUV* (GALEX), *gri* (SDSS), *JHK* (2MASS), 11 and 22 μm (WISE), 100 and 160 μm (PACS) and 250, 350, 500 μm (SPIRE), and have Hα imaging data and Balmer absorption line indices from integrated spectroscopy. Systematic effects due to different sensitivities in the various bands should thus be minimal.

3.1. Photometry

An accurate determination of the physical properties of galaxies through an SED modelling technique requires a full sampling of the electromagnetic spectrum from the UV bands (recent star formation activity) to the near- (bulk of the stellar mass), mid- (dust attenuation), and far-infrared (dust mass; e.g. Boselli 2011). The HRS has been covered at all wavelengths for this purpose. Ultraviolet data in the *FUV* (λ1539 Å) and *NUV* (λ2316 Å) have been collected thanks to two dedicated GALEX surveys (Boselli et al. 2011; Cortese et al. 2012b). Optical data in the *gri*-bands have been extracted from the SDSS (Cortese et al. 2012b) and near-IR *JHK* data from 2MASS (Skrutskie et al. 2006). Mid-IR data are available from the WISE (11 and 22 μm) and *Spitzer* (IRAC 8 μm) space missions (Ciesla et al. 2014). The sample has also been observed in the far-IR with PACS (100−160 μm; Cortese et al. 2014) and SPIRE (250−350−500 μm; Ciesla et al. 2012) on *Herschel*, while MIPS-*Spitzer* data (at 24 and 70 μm) are available only for a fraction of the sample (Bendo et al. 2012). Narrow-band Hα+[NII] imaging data are available for the vast majority of the star-forming galaxies of the sample (Boselli et al. 2015). The uncertainty in the different photometric bands slightly changes from galaxy to galaxy, as shown in the original papers where the data are published. Typical uncertainties are given in Table 2.

3.2. Spectroscopy

Age-sensitive absorption Balmer line indices have been extracted from the integrated medium-resolution ($R \simeq 1000$) spectra of the star-forming (Boselli et al. 2013) and quiescent (Gavazzi et al. 2004) galaxies of the HRS. These spectra, which cover the 3500−7000 Å spectral domain, have been obtained by drifting the slit of the spectrograph over the disc of galaxies. These spectra are thus representative of the whole galaxies and

Table 2. Uncertainties in the different photometric and spectroscopic bands.

Band	Instrument	Uncertainty	Ref.
FUV	GALEX	15%	1
NUV	GALEX	15%	1
g	SDSS	15%	1
r	SDSS	15%	1
i	SDSS	15%	1
J	2MASS	15%	2
H	2MASS	15%	2
K	2MASS	15%	2
8 μm[a]	IRAC/*Spitzer*	15%	3
11 μm	WISE	6%	3
22 μm	WISE	13%	3
24 μm[a]	MIPS/*Spitzer*	4%	4
70 μm[a]	MIPS/*Spitzer*	10%	4
100 μm	PACS/*Herschel*	16%	5
160 μm	PACS/*Herschel*	12%	5
250 μm	SPIRE/*Herschel*	6%	6
350 μm	SPIRE/*Herschel*	8%	6
500 μm	SPIRE/*Herschel*	11%	6
Hα	SPM	15%	7
Hβ	OHP	15%	8
Hγ	OHP	15%	8
Hδ	OHP	15%	8

Notes. [(a)] Available only for a fraction of the analysed galaxies.

References. (1) Cortese et al. (2012b); (2) Jarrett et al. (2003); (3) Ciesla et al. (2014); (4) Bendo et al. (2012); (5) Cortese et al. (2014); (6) Ciesla et al. (2012); (7) Boselli et al. (2015); (8) Boselli et al. (2013).

can be combined in the SED fitting analysis with the photometric data without any aperture correction. To remove the contribution of emission lines, the reduced spectra are fitted using the GANDALF code (Sarzi et al. 2006; Falcon-Barroso et al. 2006) as described in Boselli et al. (2015). This code has been designed to simultaneously fit the emission and absorption lines to properly separate the relative contribution of the stellar continuum from the nebular emission in the spectra of galaxies. When the contribution of the emission lines is removed, the stellar continuum spectra are normalised[1] to match the total emission of galaxies using the monochromatic g-band flux density of Cortese et al. (2012b) by convolving the spectrum with the SDSS g-band filter transmissivity.

3.3. Corollary data

The activity of star formation in galaxies is tightly connected to their total gas content (Boselli et al. 2001). The interaction of galaxies with the hostile cluster environment removes the gaseous component, and the lack of gas induces a quenching of the star formation activity. We therefore compare the star formation properties of the sample galaxies to their amount of gas. Atomic and molecular gas data for the large majority of the sample have been collected and homogenised in Boselli et al. (2014a). Atomic gas masses are used to derive the HI-deficiency parameter $HI-def$, which is defined as the difference in logarithmic scale between the expected and the observed HI mass of a galaxy of given angular size and morphological type (Haynes & Giovanelli 1984). The HI-deficiency for all the HRS galaxies given in Boselli et al. (2014a) has been determined using the recent calibration of Boselli & Gavazzi (2009).

HI data are also important for measuring the rotational velocity of the target galaxies, an essential parameter in the following analysis (see Sect. 4).

4. SED modelling

4.1. Models

The observed SED of the HRS galaxies are fitted using the CIGALE[2] SED modelling code (Noll et al. 2009; Ciesla et al. 2016; Boquien et al., in prep.). Its application to the HRS galaxies has been described in detail in Ciesla et al. (2014, 2016). Here we briefly summarise the main properties of this code. CIGALE produces synthetic UV to far-infrared SED of galaxies using different stellar population synthesis models available in the literature to trace the stellar emission and different dust models or empirical templates to trace the dust emission. The stellar and dust emissions are related by the dust attenuation, which is estimated taking into account an energetic balance between the energy emitted by the different stellar populations absorbed by dust and re-emitted in the infrared. The model spectra are constructed assuming different star formation histories, metallicities, and attenuation laws (see below). They are then compared to the multifrequency observations after they have been convolved with the transmissivity profile of different photometric bands that are generally used in ground-based and space missions. The code identifies the best-fit model through a χ^2 minimisation and makes a probability distribution function (PDF) analysis to identify the likelihood-weighted mean value and standard deviation for different physical parameters such as the stellar mass and the star formation rate. This code has been successfully used to reconstruct the star formation history of high-z and local galaxies (Buat et al. 2014; Boquien et al. 2016; Lo Faro et al., in prep.), including those of the HRS (Boquien et al. 2012, 2013; Ciesla et al. 2014, 2016).

The novelty introduced in this work is that we include in the fitted variables widely used age-sensitive spectral features extracted from medium-resolution ($R \sim 1000$) spectra. For this purpose, we used the high-resolution version of the Bruzual & Charlot population synthesis models (Bruzual & Charlot 2003). Consistently with our previous works, the far-infrared part of the spectrum was fitted with an updated version of the Draine & Li (2007) physical models of dust emission. These models are characterised by different variables tracing the dust properties: $q_{\rm PAH}$, the fraction of the total dust mass in PAHs containing fewer than 10^3 C atoms, $U_{\rm min}$, the intensity of the diffuse interstellar radiation field, and γ, the fraction of dust heated by young stars within photodissociation regions (PDRs), as extensively described in Draine & Li (2007) and Draine et al. (2007).

4.2. Parametrisation of the star formation history

Several observational properties of local galaxies, including SED, colour and metallicity gradients, and different scaling relations, are well reproduced assuming that galaxies are coeval systems and evolved following a delayed star formation history

[1] Because of the drifting observing technique, the spectra do not give absolute fluxes.

[2] http://cigale.lam.fr/

Table 3. Coefficients of the parametric star formation history.

Velocity km s^{-1}	a	b	c
40	4.73	–0.11	0.79
50	5.28	0.03	0.68
60	5.77	0.16	0.57
70	6.21	0.29	0.47
80	6.62	0.41	0.36
90	6.99	0.51	0.27
100	7.34	0.61	0.18
150	8.74	0.98	–0.20
220	10.01	1.25	–0.55
290	10.82	1.36	–0.74
360	11.35	1.37	–0.85

(Sandage 1986; Boissier & Prantzos 2000; Boselli et al. 2001; Gavazzi et al. 2002b). Different delayed star formation histories have been proposed in the literature. In this work we adopted the model derived by Buat et al. (2008) to reproduce the star formation history of the multizone chemo-spectrophotometric models of galaxy evolution of Boissier & Prantzos (2000). These models have been successful in reproducing the colour, metallicity, and gas radial profiles of nearby galaxies such as those analysed in this work and their typical scaling relations at different redshift (e.g. Boissier & Prantzos 2000, 2001; Boissier et al. 2001, 2003; Munoz-Mateos et al. 2007, 2009, 2011). This star formation history is parametrised with a polynom of the form

$$\log SFR(t)_{\rm secular} = a + b \log t + ct^{0.5}, \quad (1)$$

where t is the time elapsing after the first generation of stars are formed, and the coefficients a, b, and c for different rotational velocities are given in Table 3, the rotational velocity being the free parameter. A finer grid of a, b, and c coefficients has been determined by interpolating the values given in Table 3 in the velocity range 40−360 km s^{-1}.

Following this star formation history, the bulk of stars in massive galaxies is formed at early epochs, while in dwarf systems the star formation activity still increases. This parametrisation has been preferred to other analytical forms because the main parameter that regulates the secular evolution of galaxies, the rotational velocity, is an observable available for the sample galaxies. This observable is crucial to constrain the secular evolution of the target galaxies independently of the spectrophotometric data, and therefore using it reduces any possible degeneracy in the determination of the present star formation rate, quenching age, and quenching factor of the target galaxies. To check whether this assumption does not introduce any systematic bias in the results, we perform the same analysis as presented in this and the following sections in Appendix A and also leave the rotational velocity as a free parameter, and we show that our results are reliable. The rotational velocity was derived from the HI line width WHI measured using single-dish observations and reported in Boselli et al. (2014a) through the relation

$$vel_{\rm rot} = \frac{WHI}{2 \times \sin(incl)}, \quad (2)$$

where $incl$ is the inclination of the galaxy[3]. For galaxies with an inclination $incl \leq 30°$ or galaxies without HI data, the rotational velocity was derived using the stellar mass Tully-Fisher relation[4] determined for the late-type galaxies of the HRS using the set of data given in Boselli et al. (2014a; see Fig. 1). This relation is (linear fit)

$$vel_{\rm rot}\ [\rm km\ s^{-1}] = 68.71 \pm 4.17 \times \log M_{\rm star}\ [M_\odot] - 516.11 \pm 39.68 \quad (\rho = 0.75) \quad (3)$$

(where ρ is the correlation coefficient) and was derived using 217 galaxies of the sample with available data[5]. For the early-type galaxies of the sample, the rotational velocity was tentatively derived from the same stellar mass-rotational velocity relation derived for late-type galaxies (den Heijer et al. 2015). Although early-type systems do not follow the same scaling relations as spirals, this assumption is justified because we wish to test whether these typical cluster objects have been formed through the transformation of star-forming systems after a gas-stripping phenomenon.

To reproduce the quenching of the star formation activity of the Virgo cluster galaxies, we used a formalism similar to the one proposed in Ciesla et al. (2016), that is, we applied an instantaneous truncation of the star formation history parametrised by the expression

$$SFR(t) = \begin{cases} SFR(t)_{\rm secular} & \text{if } t_0 - t \geq QA \\ (1 - QF) \times SFR(t_0 - QA)_{\rm secular} & \text{if } t_0 - t < QA, \end{cases} \quad (4)$$

where $SFR(t)_{\rm secular}$ is the star formation rate expected for a secular evolution (Eq. (1)), QA is the quenching age, QF the quenching factor, and t_0 the age of the Universe at the present epoch, as depicted in Fig. 2. This is obviously a crude representation of the physical process affecting galaxies. It is indeed known from observations and simulations that the gas-stripping process is not

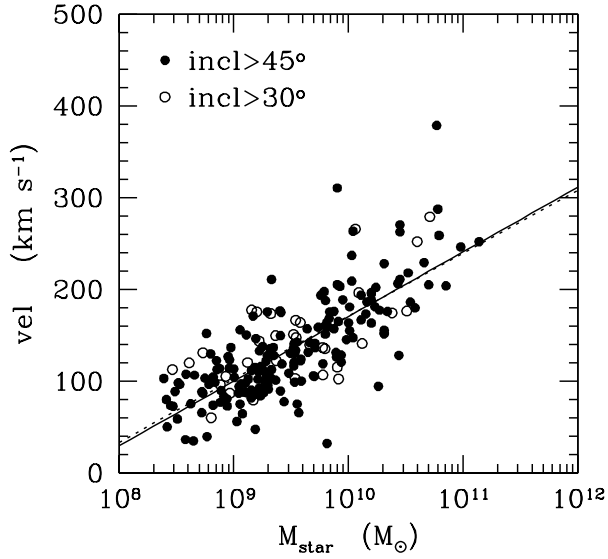

Fig. 1. Rotational velocity vs. stellar mass relation derived for HRS galaxies with an inclination $incl > 45°$ (filled dots) and $incl > 30°$ (filled and empty dots). The solid and dotted lines indicate the linear best fit to the data for galaxies with $incl > 45°$ and $incl > 30°$, respectively.

[3] The factor 2 takes into account the fact that WHI is the total (receding plus approaching) HI line width.

[4] The stellar mass relation has been preferred to the baryonic Tully-Fisher relation because molecular gas masses are not available for the low-mass galaxies of the sample.

[5] The relation does not change significantly when the fit is restricted to a smaller sample of galaxies with $incl > 45°$.

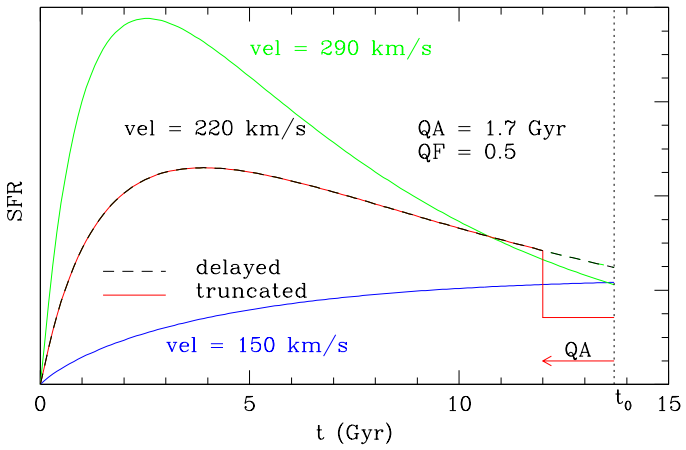

Fig. 2. Parametric star formation history for a galaxy with a rotational velocity of 220 km s^{-1} (black dashed line), 290 km s^{-1} (green solid line) and 150 km s^{-1} (blue solid line). The black dashed line shows the delayed star formation history given in Eq. (1), the red solid line the truncated one (Eq. (4)) for the case *vel* = 220 km s^{-1} (adapted from Ciesla et al. 2016).

instantaneous, but instead requires a certain time to be efficient. Furthermore, the duration of the stripping process strongly depends on the perturbing mechanism: it is very long (several Gyr) for starvation (Boselli et al. 2006) and harassment (Moore et al. 1998), for which multiple flyby encounters of cluster galaxies are required, but relatively short for ram pressure. We prefer this simple representation to a more physically motivated parametrisation such as the one proposed in Wetzel et al. (2013), however, because we wish to reduce the number of free parameters and thus limit any possible degeneracy in the derived quantities.

Hydrodynamical simulations consistently indicate that the total amount of gas of typical cluster galaxies is removed by ram pressure in $\lesssim$1.5 Gyr (Roediger & Bruggen 2007; Tonnesen & Bryan 2009). Observations and simulations, however, also indicate that most of the gaseous component is removed on much shorter timescales because the ram pressure stripping efficiency, which scales as ρV^2 (Gunn & Gott 1972, where ρ is the density of the ICM and V the velocity of galaxies within the cluster), is at its maximum only when the galaxy is crossing the core of the cluster. This is well depicted in Fig. 3 of Vollmer et al. (2001), where the figure indicates that the efficiency of ram pressure increases by a factor of $\simeq$10 on timescales $\lesssim$100 Myr. These timescales for gas stripping and quenching of the star formation activity of Virgo cluster galaxies are comparable to those derived with independent techniques on a dozen of well-known Virgo cluster galaxies (see Sect. 5).

The parametrisation given in Eq. (4) to reproduce the truncation of the star formation activity of cluster galaxies is extreme, however. To test to which degree the results obtained in the following analysis depend on this assumption, we used as other extreme case a smooth constantly declining star formation history (see Appendix A). The main results of the analysis do not change significantly.

4.3. Spectral line indices

To constrain the typical truncation age of the star formation activity in the perturbed cluster galaxies, we added several age-sensitive spectral indices. To be used and weighted as the other broad photometric bands in the CIGALE SED fitting code, these spectral indices must be defined as photometric bands. The most

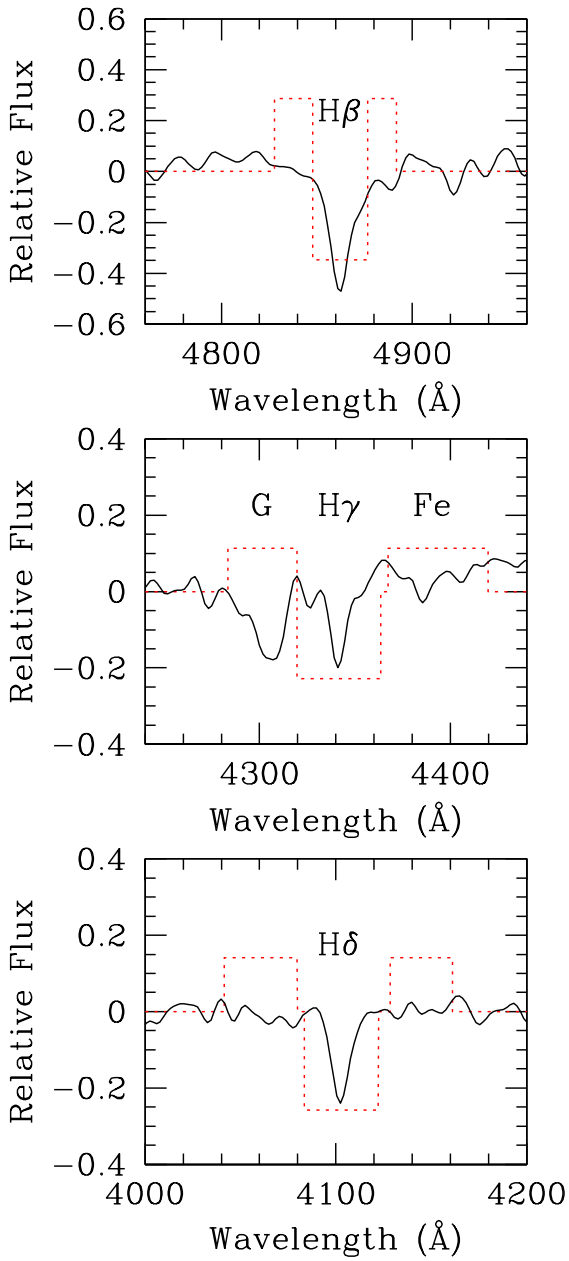

Fig. 3. Transmissivity of the newly defined pseudo-filters (red dotted line) centred on the age-sensitive Hβ, Hγ, and Hδ lines is plotted as a function of wavelength and compared to the integrated spectrum of NGC 4569 after removing the emission lines (black solid line; Boselli et al. 2013).

widely used age-sensitive spectral indices present in the visible spectra of galaxies are the Balmer absorption lines (Hβ, Hγ, Hδ) and the D_{4000} (Worthey 1994; Poggianti & Barbaro 1997; Balogh et al. 1999; Kauffmann et al. 2003; Brinchmann et al. 2004). In the standard Lick/IDS system, the Balmer indices are defined as equivalent widths. They cannot be directly used in CIGALE. We therefore defined some pseudo-filters centred on the Balmer lines where the transmissivity was set positive on the stellar continuum on the wedges of the absorption line and negative on the absorption line, as depicted in Fig. 3. The integral of the transmissivity on the blue and red stellar continua was set equal to that over the absorption line index, so that for flat spectra the

Table 4. Pseudo-filter definitions.

Filter	$\mathrm{Blue_1}$–$\mathrm{blue_2}$	$\mathrm{Line_1}$–$\mathrm{line_2}$	$\mathrm{Red_1}$–$\mathrm{red_2}$
Hβ	4827.875–4847.875	4847.875–4876.625	4876.625–4891.625
Hγ	4283.50–4319.75	4319.75–4363.50	4367.25–4419.75
Hδ	4041.60–4079.75	4083.50–4122.25	4128.50–4161.00

total flux within these pseudo-filters is zero:

$$\int_{\mathrm{blue_1}}^{\mathrm{blue_2}} T(\lambda)\mathrm{d}\lambda + \int_{\mathrm{red_1}}^{\mathrm{red_2}} T(\lambda)\mathrm{d}\lambda = -\int_{\mathrm{line_1}}^{\mathrm{line_2}} T(\lambda)\mathrm{d}\lambda \quad (5)$$

and

$$\int_{\mathrm{line_1}}^{\mathrm{line_2}} T(\lambda)\mathrm{d}\lambda = 1 \quad (6)$$

for the normalisation of the filter transmissivity, where $\mathrm{blue_1}$ and $\mathrm{blue_2}$ and $\mathrm{red_1}$ and $\mathrm{red_2}$ stand for the limits at shorter and longer wavelengths where the continuum in the Lick/IDS indices is measured, while $\mathrm{line_1}$ and $\mathrm{line_2}$ the interval in wavelengths for the absorption line[6]. The first condition is required to make the contribution of the stellar continuum on the on and off bands the same. To be as consistent as possible with the Lick/IDS definition, the continuum and the line emission were measured on the same intervals as in Worthey & Ottaviani (1997) and Worthey (1994; wide filter definition, see Table 4).

The D_{4000} spectral index generally used in the literature (e.g. Balogh et al. 1999) is defined as a ratio of the flux measured in two spectral ranges at shorter and longer wavelengths than the spectral discontinuity. Being defined as a flux ratio, this index cannot be simulated with a similarly defined pseudo-filter and was therefore not used in this analysis.

The Hα emission, which is due to the emission of the gas of the ISM ionised by the UV photons produced in O and early-B massive stars ($\gtrsim$10 $M_\odot$; Kennicutt 1998b; Boselli et al. 2009), is sensitive to much younger stellar populations ($\simeq$5 Myr; Fig. 4). Population synthesis models provide the number of ionising photons N_ν for a given star formation history. We therefore used the Hα luminosities derived from narrow-band imaging data to estimate the number of ionising photons using the relation (Osterbrock & Ferland 2006)

$$N_\nu = \frac{L(\mathrm{H}\alpha)\ [\mathrm{erg\ s^{-1}}]}{1.363\times10^{-12}}, \quad (7)$$

where L(Hα) is the Hα luminosity. Narrow-band Hα+[NII] imaging data were first corrected for [NII] contamination using the long-slit spectroscopy of Boselli et al. (2013; using the updated table given in Boselli et al. 2015). We then made the hypothesis that all the ionising radiation ($\lambda < 912$ Å) is absorbed by the gas, or in other words, that the escape fraction is zero and that the ionising photons do not contribute to the heating of dust ($f = 1$). Narrow-band Hα+[NII] imaging data were also corrected for dust attenuation. This was done using the Balmer decrement whenever possible, otherwise we used standard recipes based on monochromatic 22 μm WISE data as described in Boselli et al. (2015). CIGALE requires flux densities measured within a filter bandpass. For this reason we defined another pseudo-filter (Ly_C) to characterise the ionising radiation with a positive and constant transmissivity for $\lambda < 912$ Å:

$$\int_0^{912\ \text{Å}} T(\lambda)\mathrm{d}\lambda = 1. \quad (8)$$

[6] The transmissivity of the filter is set negative on the absorption line because the CIGALE fitting code requires positive values in the different bands.

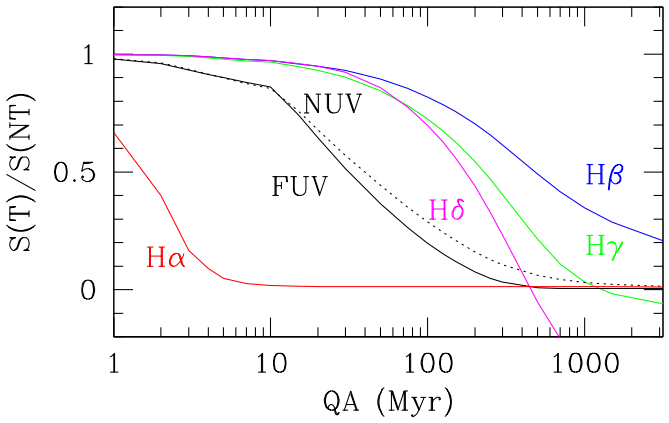

Fig. 4. Expected variation of the flux density $S(T)$ for a truncated star formation history in the FUV and NUV-bands and in the newly defined LyC (Hα), Hβ, Hγ, and Hδ pseudo-filters after a total quenching of the star formation activity (quenching factor $QF = 1$) with respect to that of an unperturbed galaxy ($S(NT)$) as a function of the quenching age QA for a model galaxy with properties given in Table 5.

Since CIGALE requires a flux density in this photometric band, the number of ionising photons must be transformed into mJy. This was done using a calibration that we derived on the mock catalogue (see Sect. 4.4) by measuring the flux density within this pseudo-filter on the SED of the simulated galaxies and comparing it to the number of ionising photons given by the population synthesis models,

$$LyC\ [\mathrm{mJy}] = \frac{1.07\times10^{-37}\times L(\mathrm{H}\alpha)\ [\mathrm{erg\ s^{-1}}]}{D^2\ [\mathrm{Mpc}]}, \quad (9)$$

or equivalently,

$$LyC\ [\mathrm{mJy}] = 1.079\times10^{4}\frac{SFR_{\mathrm{Salp}}\ [M_\odot \mathrm{yr^{-1}}]}{D^2\ [\mathrm{Mpc}]}. \quad (10)$$

Figure 4 shows the changes in flux within these newly defined pseudo-filters and in the GALEX FUV and NUV age-sensitive photometric bands when the star formation activity of a typical star forming model galaxy with parameters given in Table 5 is abruptly truncated. The Balmer absorption line indices are sensitive to stellar populations of intermediate ages and are therefore indicated to characterise the quenching age for truncations $\simeq$500 Myr old. The FUV and NUV flux densities are sensitive to relatively younger ages ($\simeq$100–200 Myr), while the number of Lyman-continuum photons derived from Hα imaging data to much younger stellar populations ($\lesssim$5 Myr; Boquien et al. 2014). The uncertainty on the flux in the pseudo-filters is hard to determine because of several factors (uncertainty on the normalisation, noise in the stellar continuum, and electronic noise in the spectrum). Similarly, the uncertainty on the number of ionised photons derived from narrow-band Hα imaging data is hardly quantifiable because of the different steps required to transform observables (Hα+[NII] fluxes) with their own uncertainties to physical quantities ([NII] contamination, dust attenuation correction, etc.). There are also large uncertainties in the stellar population synthesis models on the intensity of the Lyman-continuum photons (Levesque et al. 2012). We therefore assumed a conservative uncertainty of 15% in all the pseudo-filters but recall that the CIGALE code adds a 10% uncertainty as in all other bands. The same statistical weight is applied to all photometric bands in the fitting procedure (including the newly defined pseudo-filters).

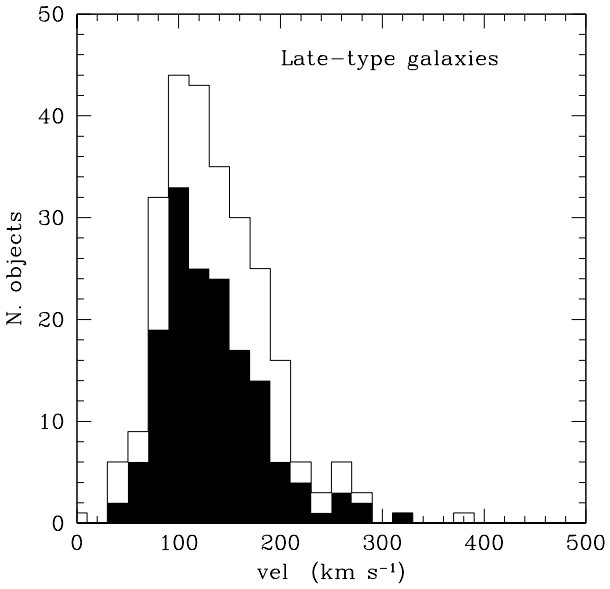

Fig. 5. Distribution of the rotational velocity of all the late-type galaxies of the sample (empty histogram) and of objects with data in the newly defined pseudo-filter bands.

Figure 5 shows the rotational velocity distribution for the late-type galaxies of the sample and indicates that the critical parameters necessary to constrain the recent star formation activity (the pseudo-filter bands as well as the FUV and NUV bands) are available for most of them. It also shows that the range in rotational velocity of the HRS galaxies is within the one covered by the star formation history given in Eq. (1) and in Table 3.

4.4. Mock catalogue of simulated galaxies

To test the solidity of this approach, we first generated a grid of simulated galaxies and extracted their SED in the same photometric and spectroscopic bands as analysed in this work by varying different input parameters in the CIGALE code, as listed in Table 5. These different parameters were chosen to sample the expected parameter space for the HRS galaxies in terms of star formation history, dust attenuation, and dust properties in a relatively uniform way. Since the most critical parameters for the following analysis are the present-day star formation rate, the star formation history, the quenching factor, and the quenching age of the perturbed galaxies, these parameters were sampled in narrower bins than the other variables in the simulated galaxies. The resulting catalogue of simulated SED includes 282 528 objects.

We then produced a mock catalogue by artificially introducing noise in the simulated SED according to the typical error in the different photometric bands. We then fitted this simulated mock catalogue of SED and made a PDF analysis of the most critical variables. To avoid edge effects in the PDF analysis, we analysed a wider range in the parameter space than in the one used to construct the SEDs. This was done only for those variables analysed in this work, that is, the quenching factor and the quenching age, as described in Table 5. Given the physical limit of the two variables (the quenching age must be ≥0 and the quenching factor cannot be >1), the PDF cannot be sampled symmetrically. We also sampled negative quenching factors that might be representative of a recent burst of star formation (see Table 5).

Figures 6–8 show the relationship between the input parameters used to define the star formation history of the simulated galaxies and the distribution of output parameters derived from SED fitting of the mock catalogue. The analysis of these figures reveals the following.

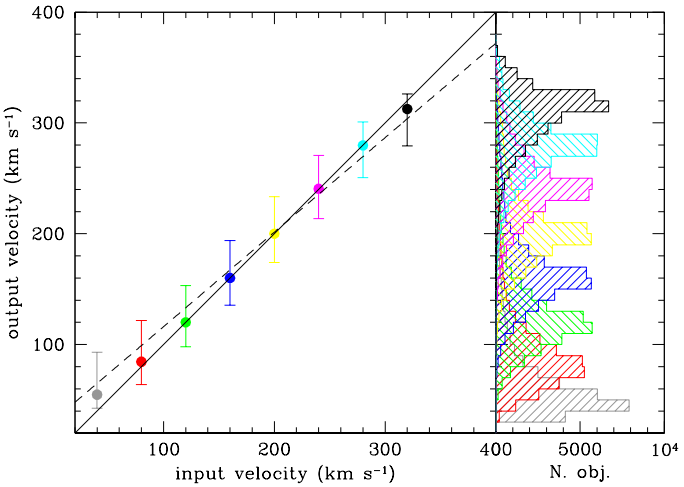

Fig. 6. Relationship between the input rotational velocity of the simulated galaxies and the output velocity derived from the PDF analysis of the mock SED (*left panel*). Dots are median values and error bars are the 16% and 84% quartiles of the distribution. The solid line shows the 1:1 relationship, and the dashed line the linear best fit to the data. The *right panel* shows the distribution of output velocities derived from the PDF analysis for a given value of the input velocity for the simulated galaxies.

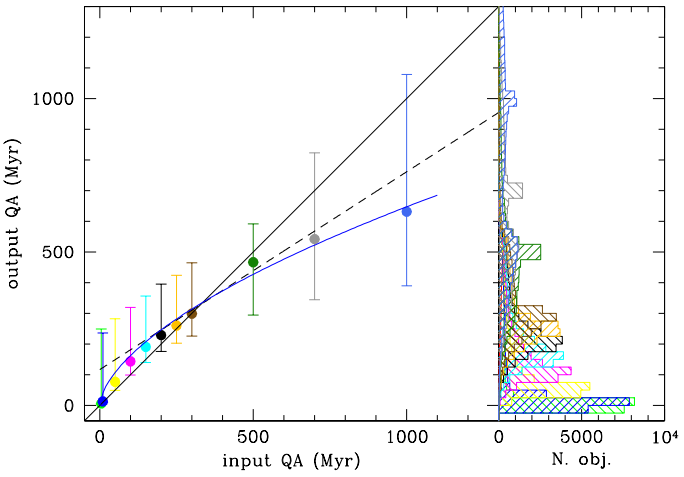

Fig. 7. Relationship between the input quenching age of the simulated galaxies and the output quenching age derived from the PDF analysis of the mock SED (*left panel*). Dots are median values and error bars are the 16% and 84% quartiles of the distribution. The solid line shows the 1:1 relationship, the dashed line the linear best fit to the data, and the blue solid line a second-degree polynomial fit. The *right panel* shows the distribution of output quenching ages derived from the PDF analysis for a given value of the input quenching age for the simulated galaxies.

(1) The rotational velocity, which is the parameter regulating the secular evolution of galaxies and thus their long-term star formation history, is well measured in the PDF analysis of the mock catalogue.
(2) The quenching age extracted from the PDF analysis matches the input values for quenching ages ≲500 Myr quite well, while it systematically underestimates the input value for older quenching ages (by ∼a factor of 2 for a quenching age

Table 5. Input parameters used to create the mock catalogue as defined in Sect. 4.1.

Parameter	Value	Units
Pop. synth. mod.	Bruzual & Charlot (2003)	
Dust model	Draine & Li (2007)	
IMF	Salpeter	
Metallicity	**0.02**	
Velocity	40, 80, 120, 160, **200**, 240, 280, 320, 360	km s^{-1}
QF	–0.4, –0.2, 0, 0.2, 0.4, 0.6, 0.7, 0.8, 0.9, 0.95, **1**	
QA	0, 5, 10, 20, 50, 100, 150, 200, 250, 300, 500, 700, 1000, 1500	Myr
$E(B-V)_{\rm young}$	0.05, 0.1, 0.2, **0.4**	
$E(B-V)_{\rm old}$	**0.44**	
$Q_{\rm PAH}$	0.47, 2.50, **4.58**, 6.63	
$U_{\rm min}$	0.1, 0.5, **2.0**, 4.0, 8.0, 20	
α	**2.5**	
γ	0.01, **0.03**, 0.1	

Notes. Parameters for the model galaxy used to trace the variation of the flux densities in the pseudo-filters after a total quenching of the star formation activity shown in Fig. 4 are given in boldface.

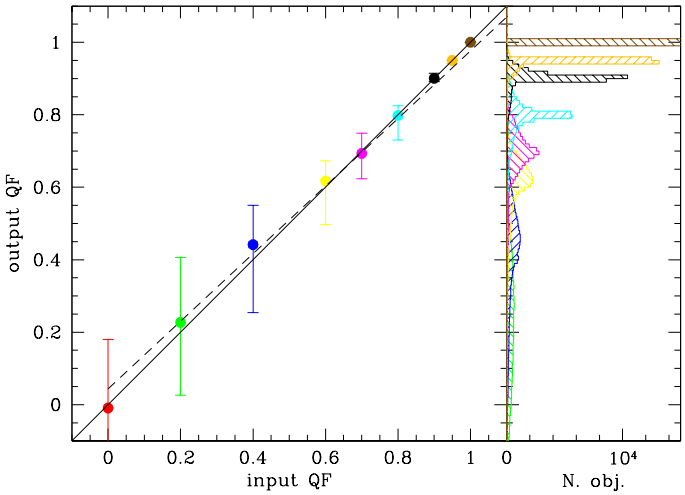

Fig. 8. Relationship between the input quenching factor of the simulated galaxies and the output quenching factor derived from the PDF analysis of the mock SED (*left panel*). Dots are median values and error bars are the 16% and 84% quartiles of the distribution. The solid line shows the 1:1 relationship and the dashed line the linear best fit to the data. The *right panel* shows the distribution of output quenching factor derived from the PDF analysis for a given value of the input quenching factor for the simulated galaxies.

of 1 Gyr). The uncertainty on the derived parameter increases with increasing input quenching ages.

(3) The quenching factor extracted from the PDF analysis is tightly connected to the input value. The uncertainty on its measure, however, increases with decreasing quenching factor. Points (2) and (3) can be understood if we consider that whenever the truncation occurred at early epochs (large QA) and/or the quenching factor is small, the imprints of these effects on the SED are hardly distinguishable from those due to possible variations in the secular evolution of galaxies. When we limit for instance the comparison of the input quenching age of the simulated galaxies and the output quenching age derived from the PDF analysis of the mock SED to those galaxies with $QF > 0.5$, that is, to those objects where the truncation of the star formation activity is significant, we obtain significantly better results (see Fig. 9).

We previously analysed the reliability of using a SED fitting analysis to study short-term variations in the star formation activity of perturbed galaxies in Ciesla et al. (2016). The results of our analysis are directly comparable since they are based on the same sample of galaxies and on the same set of photometric data. Ciesla et al. (2016) have shown that whenever UV data are available, the SED fitting analysis gives a reliable estimate of the quenching factor, but fails to estimate the quenching age and $\tau_{\rm main}$, the typical timescale characterising the secular evolution of galaxies. As discussed in Ciesla et al. (2016), this is probably due to a degeneracy between the free parameters characterising the parametrised star formation history. To overcome this problem and capitalise on the promising results obtained in Ciesla et al. (2016), we adopted here a different star formation history where the secular evolution of galaxies is not a free parameter as in Ciesla et al. (2016; the $\tau_{\rm main}$ parameter), but instead is observationally constrained from the rotational velocity of the galaxy as derived from HI data (see Sect. 4.2). The number of free parameters necessary to parametrise the star formation history is thus reduced from three to two. At the same time, we used significantly more age-sensitive photometric bands (LyC, FUV, NUV, Hβ, Hγ, Hδ) than in Ciesla et al. (2016) (FUV, NUV). In particular, the introduction of the number of ionising photons derived from the Hα emission, which are produced in young ($\lesssim 10^7$ yr) and massive ($M \gtrsim 10\ M_\odot$) stars, is critical to constrain recent episodes of star formation. These improvements reduce the degeneracy between the fitted parameters and have a significant effect on the reliability of their determination. The comparison of Figs. 7 and 8 with Figs. 4 and 5 of Ciesla et al. (2016) clearly indicates a remarkable increase in the accuracy in the quenching parameters derived in the present work.

5. SED fitting of representative galaxies

The reliability of the output parameters of our SED fitting code can additionally be tested by comparing them to those derived with independent techniques on a few well-known galaxies of the sample. A dozen of Virgo cluster galaxies of the HRS have been studied in great detail using a combination of spectro-photometric and kinematic data with models tuned to reproduce the interaction of galaxies with the hostile cluster environment.

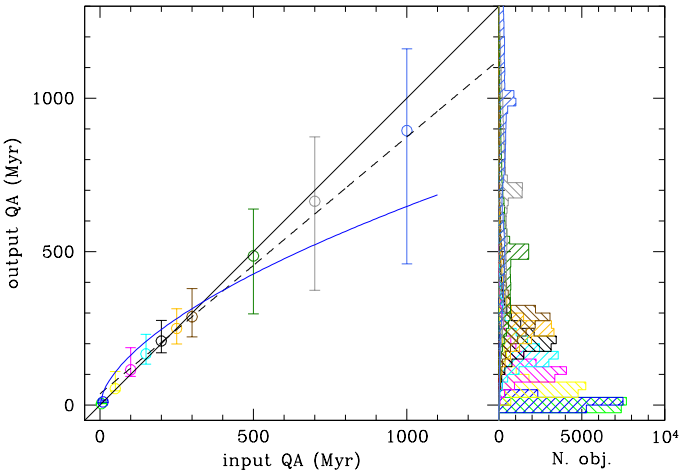

Fig. 9. Relationship between the input quenching age of the simulated galaxies and the output quenching age derived from the PDF analysis of the mock SED restricted to galaxies with an input quenching factor $QF > 0.5$ (*left panel*). Dots are median values and error bars are the 16% and 84% quartiles of the distribution. The solid line shows the 1:1 relationship, the dashed line the linear best fit to the data, and the blue solid line a polynomial fit derived for the whole mock sample shown in Fig. 8. The *right panel* shows the distribution of output quenching ages derived from the PDF analysis for a given value of the input quenching age for the simulated galaxies.

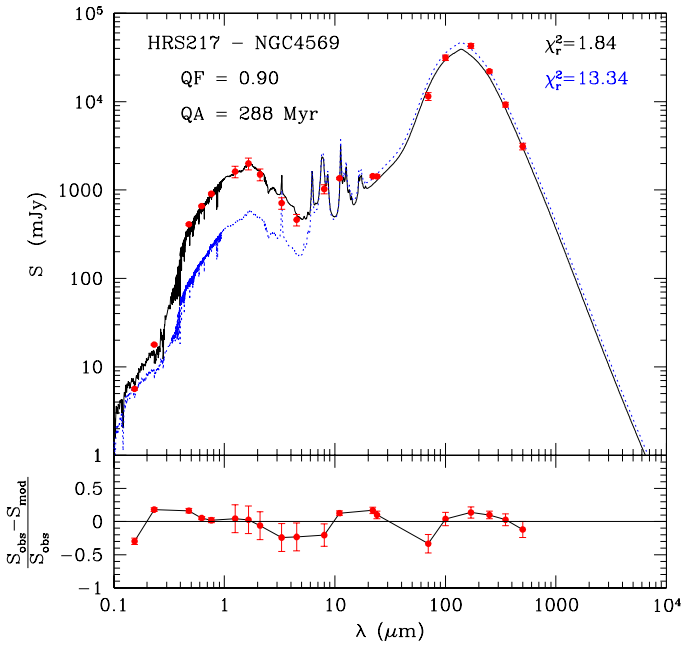

Fig. 10. Observed UV to FIR SED of NGC 4569 (HRS 217) (red filled dots) is compared to the best-fit model derived by CIGALE using a truncated star formation history (black solid line) or a normal delayed star formation history (blue dotted line) (*upper panel*). The normalised difference between the observed and model value in the different photometric bands is plotted vs. lambda in the *lower panel* (for a truncated star formation history).

5.1. NGC 4569

We first tested the reliability of our fitting procedure using NGC 4569, the brightest late-type galaxy of the Virgo cluster. This galaxy is undergoing a ram pressure stripping event, as revealed by the dynamically perturbed velocity field of the gaseous component (Vollmer et al. 2004) and the truncated gaseous and stellar disc in the young stellar populations (Hα, *FUV*, *NUV*), together with a normal extended disc in the old stellar populations (Boselli et al. 2006) and a ~100 kpc extended tail of ionised gas that formed during the interaction with the hot and dense ICM (Boselli et al. 2016). The dynamical models of Vollmer et al. (2004) indicate that the gas-stripping process took place ~300 Myr ago. Using tuned models of galaxy evolution especially tailored to take into account the effects of ram pressure stripping, Boselli et al. (2006) were able to reproduce the observed radial truncation in the gaseous disc and in the stellar disc at different wavelengths assuming that the peak of the stripping process occurred ~100 Myr ago. By studying the stellar population properties of the outer disc of NGC 4569 using IFU spectroscopic data, Crowl & Kenney (2008) concluded that the star formation activity of NGC 4569 ended outside the truncation disc ~ 300 Myr ago. We thus have consistent and independent indications that this galaxy was perturbed recently (100–300 Myr). The models of Boselli et al. (2006) also indicate that the activity of star formation of this galaxy was reduced by 95% ($QF = 0.95$).

The observed UV to FIR SED of NGC 4569 is well reproduced by CIGALE using a truncated star formation history, while the fit does not match the photometric data in the UV to NIR bands when a simple delayed star formation history is adopted (Fig. 10). The match between the best model and the observations is also evident at high resolution in the optical domain, where the truncated model can be directly compared to the normalised observed spectrum (Fig. 11). Despite a systematic shift in the model vs. observations that is present in the UV to FIR SED in the g band used for the normalisation of the integrated spectrum, there is a very good agreement in the high-resolution absorption features, and in particular in the age-sensitive Balmer absorption lines used in the fit.

Our SED fitting code gives $QA = 288 \pm 23$ Myr and a $QF = 0.90 \pm 0.05$, values very consistent with those derived with independent techniques. NGC 4569 also belongs to the SINGS sample of galaxies (Kennicutt et al. 2003) and thus has an integrated spectrum taken by Moustakas et al. (2010). When we combine the photometric data with the spectroscopic dataset of Moustakas et al. (2010), we derive very similar values for the quenching age ($QA = 299 \pm 15$ Myr) and the quenching factor ($QF = 0.90 \pm 0.05$), indicating that the derived values are robust vs. the use of different spectroscopic datasets.

5.2. Other galaxies

The same comparison can be extended to a few other galaxies with estimates of the quenching age from dynamical models or from IFU spectroscopic data of the outer discs (see Fig. 12 and Table 6). We recall that the timescales derived using dynamical models indicate the epoch when the gaseous component started to be perturbed. This might not coincide with the beginning of the decrease of the star formation activity, which generally occurs after the gas has been stripped (Boselli et al. 2008; Crowl & Kenney 2008). Furthermore, the analytical definition of the star formation history used in this work does not allow negative quenching ages as dynamical models do (the gas-stripping process starts before the peak of the ram-pressure-stripping process has been reached). Despite the large uncertainty in the plotted parameters, the quenching ages derived using different techniques agree well overall when the comparison is limited to objects with a good quality fit (reduced $\chi^2_r \leq 3$).

Table 6. Quenching parameters derived using other techniques for some HRS galaxies in the Virgo cluster.

HRS	NGC/IC	*Vel*	*QA*	*QF*	χ^2_r	Age	Ref.	Method
		km s^{-1}	Myr			Myr		
(1)	(2)	(3)	(4)	(5)	(6)	(7)	(8)	(9)
102	4254	175	129 ± 478	–0.06 ± 0.36	3.14	280	8	dyn
124	4330	120	172 ± 50	0.89 ± 0.04	1.09	–100	3	dyn
124	4330	120	172 ± 50	0.89 ± 0.04	1.09	200–400	11	phot
144	4388	180	61 ± 25	0.74 ± 0.06	1.00	225 ± 100	6	spec
144	4388	180	61 ± 25	0.74 ± 0.06	1.00	120	9	dyn
149	4402	120	1302 ± 320	0.90 ± 0.04	3.23	200^a	6	spec
156	4419	95	1610 ± 75	0.95 ± 0.05	6.15	500 ± 150	6	spec
159	4424	32	501 ± 25	0.95 ± 0.05	2.81	275 ± 75	6	spec
163	4438	130	576 ± 250	0.95 ± 0.05	3.66	100	4	dyn
172	IC3392	100	299 ± 15	1.0 ± 0.05	2.90	500 ± 100	6	spec
190	4501	290	77 ± 135	0.81 ± 0.09	2.88	–250	7	dyn
197	4522	105	64 ± 101	0.80 ± 0.04	3.01	50	5	dyn
197	4522	105	64 ± 101	0.80 ± 0.04	3.01	100 ± 50	6	spec
217	4569	220	288 ± 23	0.90 ± 0.05	1.84	100	1	model
217	4569	220	288 ± 23	0.90 ± 0.05	1.84	300	2	dyn
217	4569	220	288 ± 23	0.90 ± 0.05	1.84	300 ± 50	6	spec
221	4580	105	646 ± 101	0.95 ± 0.05	1.52	475 ± 100	6	spec
247	4654	175	645 ± 804	0.40 ± 0.21	2.39	500^a	10	dyn

Notes. $^{(a)}$ Upper limit. Column 1: HRS name; Col. 2: NGC/IC name; Col. 3: rotational velocity used in the CIGALE fit; Col. 4: *QA* and error derived using CIGALE; Col. 5: *QF* and error derived using CIGALE; Col. 6: reduced χ^2_r; Col. 7: age of the interaction derived in the literature; Col. 8: references coded as: 1: Boselli et al. (2006); 2: Vollmer et al. (2004); 3: Vollmer et al. (2012); 4: Vollmer et al. (2009); 5: Vollmer et al. (2006); 6: Crowl & Kenney (2008); 7: Vollmer et al. (2008a); 8: Vollmer et al. (2005); 9: Vollmer & Huchtmeier (2003); 10: Vollmer (2003); 11: Abramson et al. (2011); Col. 9: method used to derive the age of the interaction: "dyn" stands for dynamical models based on the HI and/or CO data; "spec" for IFU spectroscopy of the outer stellar disc; "model" for multizone-chemospectrophotometric models of galaxy evolution; "phot" derived using UV-to-optical photometry.

Table 7. Input parameters used to fit the HRS galaxies.

Parameter	Value	Units
Pop. synth. mod.	Bruzual & Charlot (2003)	
Dust model	Draine & Li (2007)	
IMF	Salpeter	
Metallicity	0.02	
Velocity	40–360 in step of 10	km s^{-1}
QF	–0.4, –0.2, 0.2, 0.4, 0.6, 0.7, 0.8, 0.9, 0.95, 1	
QA	0, 5, 10, 20, 50, 100, 150, 200, 250, 300, 400, 500, 600, 700, 800, 900, 1000, 1250, 1500, 2000, 3000	Myr
$E(B-V)_{\rm young}$	0.05, 0.1, 0.2, 0.4	
$E(B-V)_{\rm old}$	0.44	
$Q_{\rm PAH}$	0.47, 2.50, 4.58, 6.63, 7.32	
$U_{\rm min}$	0.1, 0.5, 2.0, 4.0, 8.0, 20	
α	2.0, 2.5, 3.0	
γ	0.01, 0.03, 0.1	

Notes. The input parameters used in the analysis of the HRS span a wider range than those used to create the mock galaxies to avoid border effects.

6. SED fitting of the HRS

Since we wish to focus our analysis on the quenching phenomenon, the model SED used in the following analysis were constructed using the appropriate rotational velocity as derived from kinematical data for each galaxy (or from the Tully-Fisher relation as explained in Sect. 4.2 whenever the former is not available). The grid of parameters used to fit the observed data is listed in Table 7.

Figure 13 shows the relationship between the flux densities in the four pseudo-filters derived from the PDF analysis vs. the one measured on the observed spectra. The correlation between the two variables is excellent in the Hβ and Hδ bands, while the

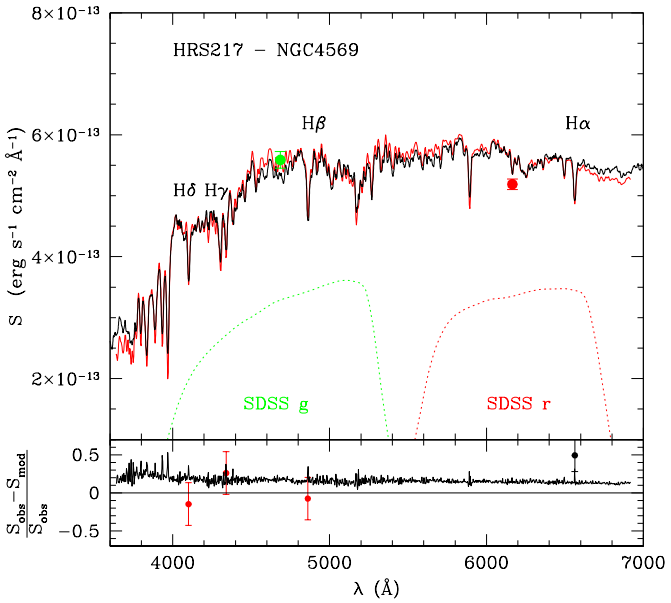

Fig. 11. Integrated spectrum of NGC 4569, with a resolution of $R \sim 1000$, corrected for line emission (red line), normalised to the flux density in the g band (green filled dot), compared to the best-fit model derived by CIGALE using a truncated star formation history (black solid line; the model spectrum is shifted on the Y-axis by a factor of $+8 \times 10^{-14}$ to match the observed spectrum). The red filled dot shows the r-band photometric point, and the transmissivity of the SDSS g and r bands is traced by the green and red dotted curves (*upper panel*). The normalised difference between the two spectra is plotted vs. lambda in the *lower panel*. The red filled dots indicate the normalised difference between the values of the Hβ, Hγ, and Hδ pseudo-filters and those measured on the best-fit model. The black filled dot at λ6563 Å shows the normalised difference between the observed Lyman-continuum pseudo-filter, derived from the extinction-corrected Hα image of the galaxy, and the Lyman-continuum flux measured on the best-fit model.

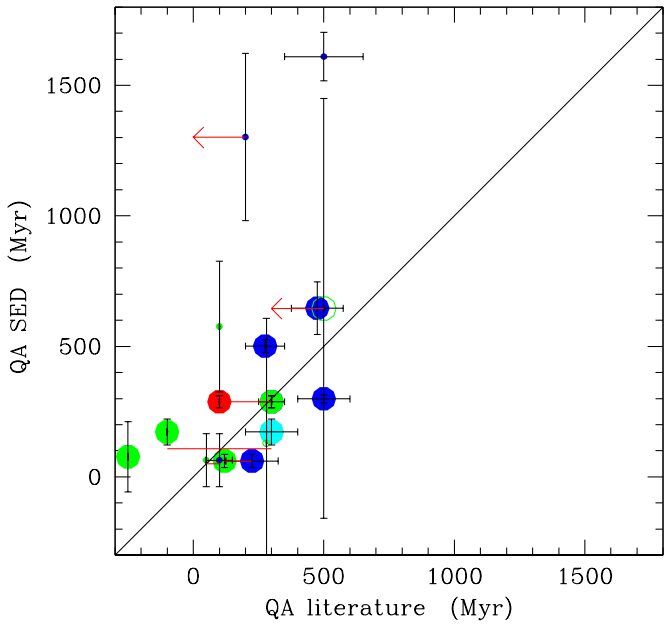

Fig. 12. Relationship between the quenching age derived using our SED fitting technique and that derived using multizone chemo-spectrophotometric models of galaxy evolution for NGC 4569 (red dot), dynamical models based on the HI and CO gas kinematics (green dots), IFU spectroscopy of the outer disc of some cluster galaxies (blue dots), and photometric data compared to population synthesis models (cyan dots). Filled symbols are used for galaxies with a quenching factor $QF > 0.5$, empty dots for those with $QF \leq 0.5$. Large symbols are for galaxies with a reduced $\chi^2_r \leq 3$, small symbols for $\chi^2_r > 3$. The red lines connecting two points are used to indicate galaxies for which two independent quenching ages are available in the literature. The red arrows indicate upper limits to the quenching age given in the literature. The data used for this plot are given in Table 6. The solid diagonal line indicates the 1:1 relationship.

scatter increases in Hγ and particularly in the Lyman continuum derived from the Hα data. The low scatter in the Hβ and Hδ relations probably arises because both variables are sensitive to stellar populations of young-to-intermediate age (see Fig. 4), which are already well constrained by the FUV-to-far-IR photometric bands. The systematic difference observed in the Hγ pseudo-filter might result from a possible contamination of the Fe and G-bands in the stellar continuum (see Fig. 3). The large scatter in the Lyman-continuum pseudo-filter probably arises because this is the only photometric band sensitive to very young ($\lesssim 10^7$ yr) stellar populations. It is therefore the most critical (and unique) band for constraining recent variations in the star formation activity of the galaxies. The correlation between the two variables is excellent whenever $QF \leq 0.5$ (mainly unperturbed objects), while there is a systematic difference for the most perturbed galaxies ($QF > 0.8$). The systematic variation of the correlation with QF seen in Fig. 13 might be an artefact that is due to the very simplistic parametrisation of the star formation law used to describe the quenching phenomenon (Eq. (4)). Another possible origin of the observed scatter in the Lyman continuum pseudo-filter might be that this observable is derived from Hα+[NII] imaging data after correcting for [NII] contamination using integrated spectroscopy and for dust attenuation using the Balmer decrement whenever possible, or the 22 μm emission from WISE otherwise (Boselli et al. 2015). All these corrections are quite uncertain.

7. Analysis

To limit the uncertainty in the determination of the quenching age and quenching factor parameters, the analysis presented in this and in the following sections is restricted to the late-type galaxies of the HRS with available spectroscopic, FUV, NUV, and Hα imaging data, the last opportunely corrected for dust attenuation as described in the previous sections. We recall that for all these galaxies photometric data are also available in the gri from SDSS, JHK from 2MASS, 11 and 22 μm from WISE, 100 and 160 μm from PACS and 250, 350, 500 μm from SPIRE, while *Spitzer* data at 8, 24, and 70 μm for a large portion of the sample (see Table 2). We also analyse 22/61 of the early-type galaxies of the HRS with the same set of spectro-photometric data, with the exception of Hα imaging data, but for which an upper limit to the Hα emission has been derived from the spectra. As stated in Sect. 2, this sample includes galaxies in different density regions, from the core of the Virgo cluster to small groups, binary systems, and relatively isolated objects in the field (Boselli et al. 2010a).

We first tested whether the use of a truncated star formation history increases the quality of the SED fitting procedure of the perturbed Virgo cluster galaxies as in the case of NGC 4569 (see Fig. 10). To do that, we plot the relationship between $\chi^2_r(T)/\chi^2_r(NT)$, where $\chi^2_r(T)$ is the reduced chi-square derived using a truncated star formation history (Eq. (4)) and $\chi^2_r(NT)$ the one derived using an unperturbed star formation history (Eq. (1)), and the HI-deficiency parameter (Fig. 14), here

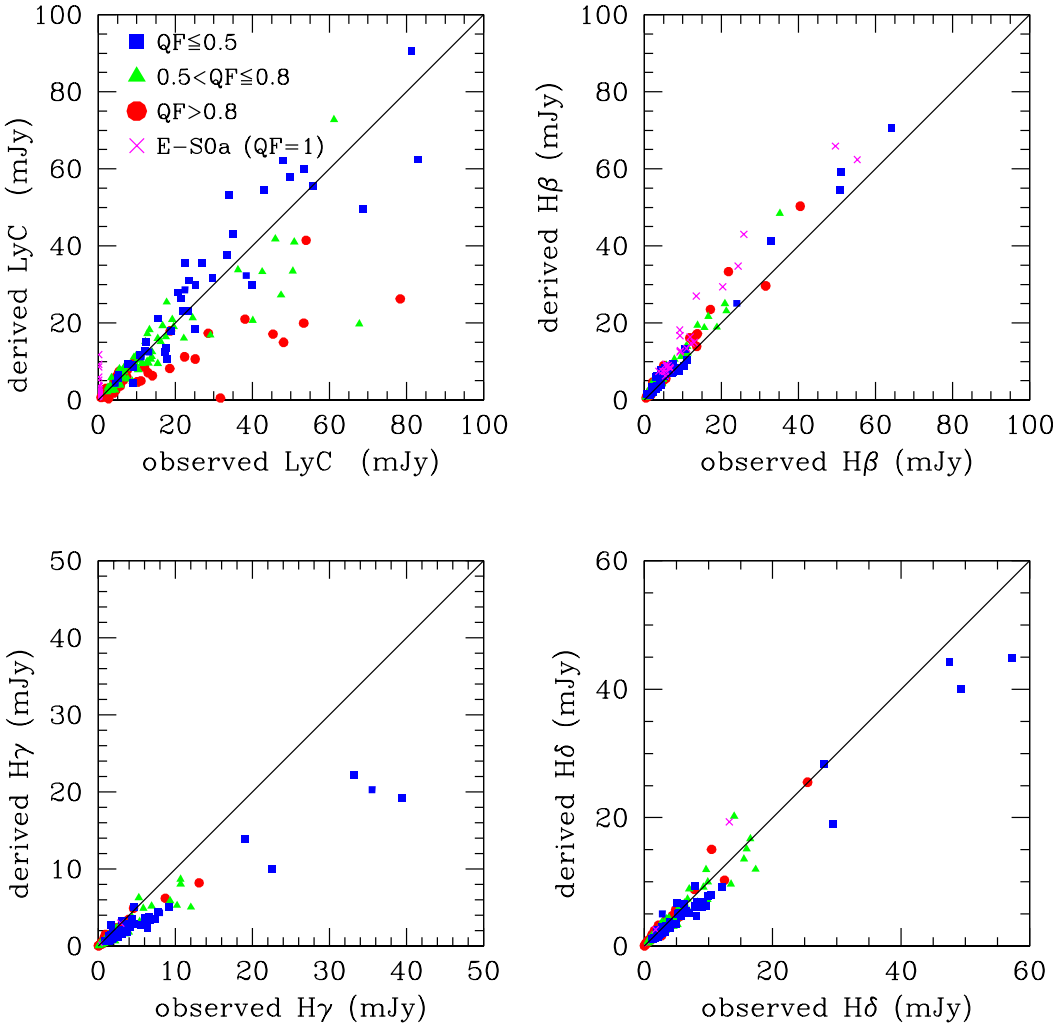

Fig. 13. Relationship between the flux densities measured within the four different pseudo-filters defined in this work on the best-fit model and those measured on the observed spectra. The solid line indicates the 1:1 relation. Blue filled squares, green triangles, red circles, and magenta crosses are for galaxies where the derived quenching factor is $QF \leq 0.5$, $0.5 < QF \leq 0.8$, $QF > 0.8$, and early-type galaxies (all with $QF = 1$), respectively.

taken as proxy for the perturbation. We recall that the typical HI-deficiency of isolated galaxies is $HI - def \lesssim 0.4$, while it increases to $HI - def \simeq 1$ in the core of the Virgo cluster.

Obviously, the use of a complex star formation history characterised by two more free parameters (QF and QA) rather than a simple secular evolution increases the quality of the fit in all galaxies ($\chi^2_r(T)/\chi^2_r(NT) \leq 1$). Figure 14 shows, however, that the quality of the fit increases significantly in the most HI-deficient galaxies of the sample ($HI - def \gtrsim 0.5$) and in objects where the quenching factor is high ($QF > 0.8$). We also tested whether QF and QA, the two free parameters that we wish to analyse in this work, are correlated, thus witnessing a possible strong degeneracy in these outputs of the model. We did not find any clear trend between these two variables.

7.1. Quenching factor

Figure 15 shows the relationship between the quenching factor QF (lower panel) and the HI-deficiency parameter. The quenching factor increases with the HI-deficiency parameter, indicating that the activity of star formation of the sample galaxies is significantly reduced when the HI gas content is removed during the interaction with the hostile cluster environment (Ciesla et al. 2016; the Spearman correlation coefficient derived for the 95 galaxies with $QF > 0.5$ and $\chi^2_r \leq 3$ is $\rho = 0.58$). The median quenching factor of HI-deficient galaxies ($HI - def > 0.4$) is $\langle QF_{HI-def>0.4} \rangle = 0.80 \pm 0.11$ for $\langle HI - def \rangle = 0.68 \pm 0.20$, roughly indicating that the activity of star formation of a perturbed galaxy is reduced by ~80% when the gas content drops by a factor of ~5. For comparison, all the early-type galaxies of the sample with available spectroscopic and UV data have a quenching factor $QF = 1$. As discussed in Appendix A, these results are independent of which star formation history is adopted.

7.2. Quenching age

Figure 15 also shows the relationship between the quenching age QA and the HI-deficiency parameter ($\rho = 0.48$). There is a clear relationship between the two variables, in particular if only those galaxies where QA is securely determined ($QF > 0.5$) are considered. The activity of star formation has been reduced ~1 Gyr ago in the most HI-deficient objects of the sample ($HI - def \gtrsim 0.8$).

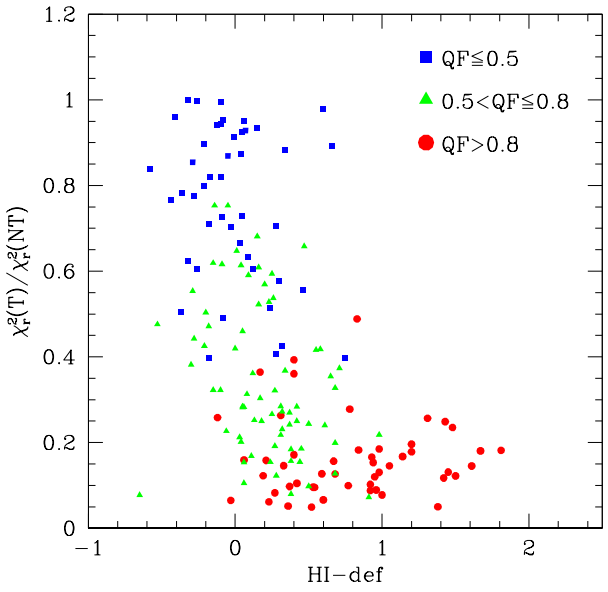

Fig. 14. Relationship between the reduced χ^2_r ratio derived using a truncated ($\chi^2_r(T)$) to a non-truncated ($\chi^2_r(NT)$) star formation history and the HI-deficiency parameter. Blue filled squares, green triangles, and red circles are for late-type galaxies with a quenching factor $QF \leq 0.5$, $0.5 < QF \leq 0.8$, and $QF > 0.8$, respectively.

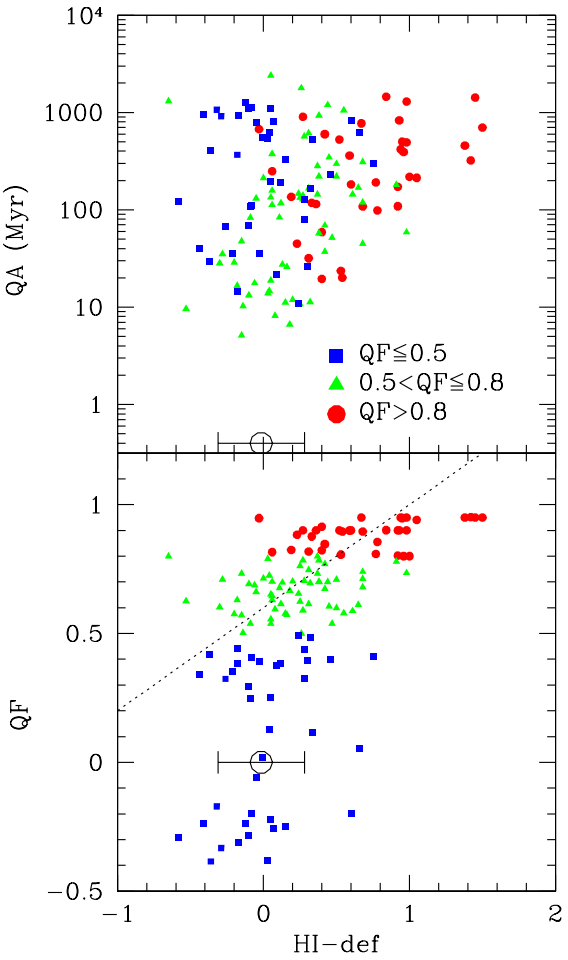

Fig. 15. Relationship between the quenching age QA (*upper panel*) and the quenching factor QF (*lower panel*) and the HI-deficiency parameter for objects with $\chi^2_r \leq 3$. Blue filled squares, green triangles, and red circles are for galaxies where the derived quenching factor is $QF \leq 0.5$, $0.5 < QF \leq 0.8$, and $QF > 0.8$, respectively. The large black empty symbol shows the mean value and the distribution in HI-deficiency for galaxies with a $QF \leq 0.5$ (for which the quenching factor and quenching age are arbitrarily set to $QF = 0$ and $QA = 0.4$ Myr). The dotted line in the lower panel indicates the best fit found by Ciesla et al. (2016).

Figure 16 shows the distribution of the quenching age parameter QA. The median quenching age of late-type galaxies is $QA = 135$ Myr for $0.5 < QF \leq 0.8$ and $QA = 250$ Myr for $QF > 0.8$, while that of early-type galaxies is $QA = 1320$ Myr (see Table A.1). As dicussed in Appendix A, these numbers do not change significantly when the SED fitting includes the rotational velocity as a free parameter. They increase by a factor of ∼2 when the quenching mechanism is parametrised with a smoothly declining star formation history.

8. Discussion

8.1. Comparison with previous studies

As discussed in Sect. 5.2, the quenching ages determined in this work are comparable to those derived using independent techniques on dozens of well-studied galaxies in the Virgo cluster. These timescales are also consistent with a rapid transformation of gas-rich systems into quiescent objects derived from the analysis of the $NUV - i$ colour magnitude relation in the Virgo cluster and its surrounding regions (Boselli et al. 2014c; see also Cortese & Hughes 2009; Hughes & Cortese 2009) and with the most recent estimates of the galaxy infall rate in the cluster (∼300 Gyr^{-1} for galaxies with $M_{\rm star} \gtrsim 10^8$ $M_\odot$, Boselli et al. 2008; Gavazzi et al. 2013a). These short timescales are also consistent with the presence of a long tail of extraplanar ionised gas associated with NGC 4569 (Boselli et al. 2016), one of the most HI-deficient Virgo cluster galaxies ($HI - def = 1.05$; Boselli et al. 2014a) characterised by a quenched star formation activity ($QF = 0.90$). The tail of ionised gas witnesses a stripping process that is still ongoing.

Direct observational evidence of a rapid quenching of the star formation activity of cluster galaxies are poststarburst objects in the periphery of nearby clusters such as Coma and A1367 (Poggianti et al. 2001a,b, 2004; Smith et al. 2008, 2009, 2012; Gavazzi et al. 2010). These objects are frequent also in other nearby (Fritz et al. 2014; Vulcani et al. 2015) and intermediate- to high-redshift clusters (Dressler et al. 1999, 2013; Balogh et al. 1999, 2011; Poggianti et al. 2004, 2009; Tran et al. 2007; Muzzin et al. 2012, 2014; Mok et al. 2013; Wu et al. 2014). The frequency of these objects with a recently truncated star formation activity increases with decreasing stellar mass (Boselli & Gavazzi 2014). Evidence of a rapid transformation at intermediate redshift comes also from the analysis of the Hα luminosity function (e.g. Kodama et al. 2004).

The analysis of large samples of nearby galaxies in different environments, from groups to massive clusters, extracted from complete surveys such as the SDSS, GALEX, or GAMA, combined with the predictions of cosmological simulations or semi analytical models of galaxy evolution, indicates that the activity of star formation gradually and moderately decreases when galaxies become satellites of more massive galaxies on relatively long timescales (2−7 Gyr; McGee et al. 2009; von der Linden et al. 2010; De Lucia et al. 2012). Similar results have also been obtained through the analysis of limited samples of nearby galaxies with available multifrequency data (Wolf et al. 2009; Haines et al. 2015; Paccagnella et al. 2016). More recent works suggest that after this mild decrease, the activity rapidly drops

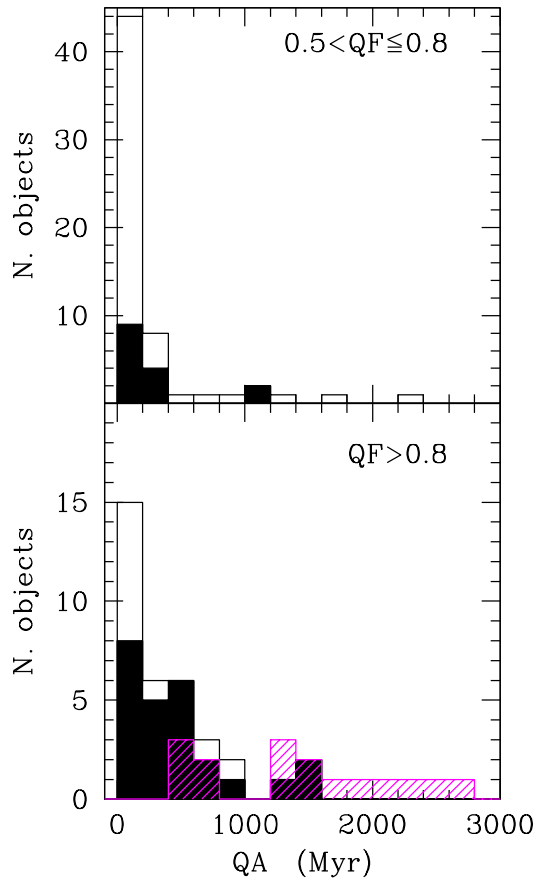

Fig. 16. Distribution of the quenching age parameter QA for galaxies with $\chi^2_r \leq 3$ and a quenching factor $0.5 < QF \leq 0.8$ (*upper panel*) and $QF > 0.8$ (*lower panel*). The magenta histogram is for early-type galaxies, the empty histogram for all late-type galaxies, and the black shaded histogram for HI-deficient ($HI - def > 0.4$) late-type systems.

on short timescales (0.2−0.8 Gyr) after the atomic and molecular gas content is consumed through star formation (Wetzel et al. 2012, 2013; Wijesinghe et al. 2012; Muzzin et al. 2012). Preprocessing in infalling groups is therefore probably important in shaping the evolution of galaxies now members of massive clusters (Dressler 2004). The only indication for a very inefficient quenching of the star formation activity (>9.5 Gyr) of dwarf galaxies ($10^{8.5} < M_{\rm star} < 10^{9.5}$ $M_\odot$) in relatively dense environments comes from the analysis of SDSS data combined with cosmological simulations reported by Wheeler et al. (2014).

8.2. Identification of the perturbing mechanism

The typical timescales derived in the previous section and in Appendix A can be compared to those predicted by models and simulations for the identification of the dominant stripping mechanism in the nearby Virgo cluster. We recall that given the analytical form of the star formation history used in this work (Eq. (4)), the quenching ages derived in the previous sections are not the typical timescales necessary to reduce the activity of star formation by a factor QF, but just the look-back time to the quenching epoch. However, since they are typically $QA \lesssim 1.3$ Gyr for $QF \leq 1$, they indicate that the timescale for quenching the activity of star formation is relatively short. This is also the case when a smoothly declining quenching process is assumed (see Appendix A).

The typical timescale for galaxy-galaxy interactions is longer than the age of the Universe in dense environments such as the Virgo cluster because of the large velocity dispersion of this massive system (Boselli & Gavazzi 2006). Galaxy harassment is more efficient than galaxy-galaxy interactions because of the contribution of the potential well of the cluster. The simulations of Mastropietro et al. (2005), tuned to reproduce a Virgo-cluster-like environment for galaxies of a few 10^9 $M_\odot$, indicate that the typical timescale necessary to heat a disc galaxy and form a pressure-supported system is a few Gyr. Unfortunately, these simulations do not make any prediction on the evolution of the star formation activity, but we can expect that these timescales are comparable to those required to heat the perturbed galaxy. Again, these timescales are longer than those derived in the previous section because the typical relaxation time in clusters such as Virgo is comparable to the age of the Universe.

In a starvation scenario, a galaxy entering a dense environment looses its halo of hot gas that stops the infall of fresh material. The activity of star formation gradually decreases after the consumption of the cold atomic and molecular gas located on the disc (Larson et al. 1980). The typical timescale for gas consumption of the HRS galaxies is ≃4 Gyr (Boselli et al. 2014d), and it drops to ≳3.0−3.3 Gyr in gas deficient objects (Boselli et al. 2014b). These timescales, however, should be considered as lower limits since the star formation activity of the perturbed galaxies gradually decreases when the gas is removed, thus extending the time during which galaxies can still form stars. Tuned models of galaxy starvation of the representative HRS galaxy NGC 4569 (Boselli et al. 2006) or of objects with a wide range of stellar masses (Boselli et al. 2014c) consistently indicate that the starvation process requires very long timescales (≳6 Gyr) to significantly reduce the star formation activity of the perturbed galaxies. Long timescales for starvation to be efficient are also indicated by numerical simulations (e.g. Bekki et al. 2002; McGee et al. 2014). This is depicted in Fig. 17, where the main-sequence diagram derived using the output parameters of the SED fitting is compared to the predictions of the evolutionary models of Boselli et al. (2006, 2008, 2014c) for starvation and ram pressure stripping. Figure 17 clearly shows that even if the process started ∼10 Gyr ago, starvation would never be able to reduce the star formation activity of the perturbed galaxies by $QF \gtrsim 0.5$.

Much shorter timescales for an efficient quenching of the star formation activity are instead predicted by hydrodynamic simulations (Roediger & Henseler 2005; Roediger & Bruggen 2006, 2007; Tonnesen et al. 2007; Tonnesen & Bryan 2009; Bekki 2009) and chemo-spectrophotometric models (Boselli et al. 2006, 2008, 2014c; Cortese et al. 2011) of ram pressure stripping in clusters of mass comparable to Virgo. The predictions of these chemo-spectrophotometric models derived for two different ram-pressure-stripping efficiencies, $\epsilon_0 = 1.2$ $M_\odot$ kpc^{-2} yr^{-1} necessary to reproduce the observed truncated profiles of the Virgo cluster galaxy NGC 4569 (Boselli et al. 2006), and $\epsilon_0 = 0.4$ $M_\odot$ kpc^{-2} yr^{-1}, the mean stripping efficiency for galaxies with the typical velocity dispersion within the Virgo cluster (Boselli et al. 2008), are compared to the data in Fig. 17. The observed decrease in the star formation activity of HI-deficient galaxies (Boselli et al. 2015) in the main sequence relation can be explained by ram pressure stripping, a result similar to the one derived from the analysis of the UV-to-optical colour magnitude relation (Cortese & Hughes 2009; Hughes & Cortese 2009; Boselli et al. 2014c,d). The large number of objects below the main sequence drawn by unperturbed systems, often taken as an indication that the perturbing process lasts several Gyr, is due

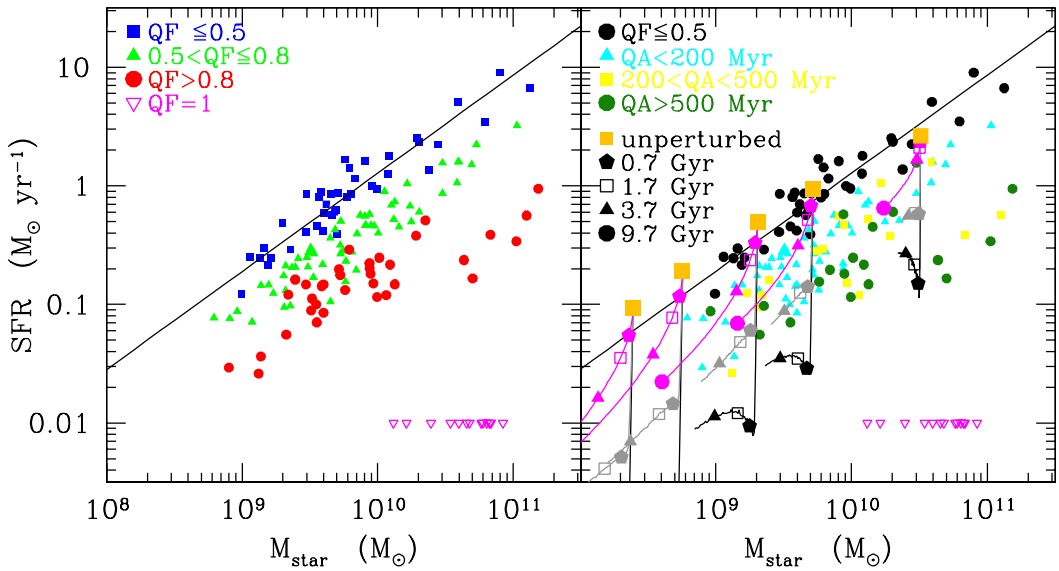

Fig. 17. Relationship between the present day star formation rate and the stellar mass (main sequence) derived from the SED fitting code. *Left panel*: symbols are coded according to the quenching factor of the analysed galaxies. Blue filled squares, green triangles, and red circles are for galaxies where the derived quenching factor is $QF \leq 0.5$, $0.5 < QF \leq 0.8$, and $QF > 0.8$, respectively. Magenta triangles indicate upper limits to the star formation rate of early-type galaxies. The solid line shows the bisector fit to the data for unperturbed galaxies ($QF \leq 0.5$). *Right panel*: same relation with colour symbols coded according to the quenching age. Black filled dots are for unperturbed galaxies ($QF \leq 0.5$), cyan triangles, yellow squares, and dark green dots for galaxies with a quenching age $QA < 200$ Myr, $200 < QA < 500$ Myr, and $QA > 500$ Myr, respectively. The large orange filled squares indicate the models of Boselli et al. (2006, 2014c) for unperturbed galaxies of spin parameter $\lambda = 0.05$ and rotational velocity 70, 100, 130, 170, and 220 km s^{-1}. The magenta lines indicate the starvation models. The black and grey lines show the ram-pressure-stripping models for a stripping efficiency $\epsilon_0 = 1.2$ $M_\odot$ kpc^{-2} yr^{-1} and $\epsilon_0 = 0.4$ $M_\odot$ kpc^{-2} yr^{-1}, respectively. Different symbols in the models indicate the position of the model galaxies at a given look-back time from the beginning of the interaction.

to the high infall rate of star-forming systems observed in Virgo (≃300 Gyr^{-1}; Tully & Shaya 1984; Boselli et al. 2008; Gavazzi et al. 2013a). Further evidence in agreement with the ram pressure stripping scenario is given in Fig. 18, where the fraction of late-type galaxies with a quenching factor $QF > 0.8$ and an HI-deficiency $HI - def > 0.4$ are plotted versus the distance from the core of the Virgo cluster. Figure 18 clearly shows that both fractions drop by a factor of ≃5 from the core of the cluster ($R/R_{\rm vir} < 0.5$), where the hot X-ray gas is detected by *ROSAT* (Bohringer et al. 1994), to the cluster periphery ($R/R_{\rm vir} \gtrsim 4$), in agreement with models and simulations (Tonnesen et al. 2007; Bahe et al. 2013; Cen et al. 2014). Recent observations of nearby clusters with 4−8 m class telescopes equipped with wide-field panoramic detectors and narrow-band filters revealed several star forming galaxies with long tails of ionised gas that are typically produced by a ram-pressure-stripping event up to the cluster virial radius (Gavazzi et al. 2001; Sun et al. 2007; Yagi et al. 2010; Fossati et al. 2012). Two galaxies with long tails of HI gas have been also observed in the periphery of A1367, outside the virial radius (Scott et al. 2012). The radial variation of the fraction of quenched and HI-deficient galaxies is consistent with the one observed in the Virgo cluster out to large distances by Gavazzi et al. (2013a) and Boselli et al. (2014c), additional evidence that quenching is a rapid process (Boselli et al. 2014c).

Short timescales are also consistent with a recent formation of the faint end of the red sequence (De Lucia et al. 2007, 2009; Stott et al. 2007, 2009; Gilbank & Balogh 2008).

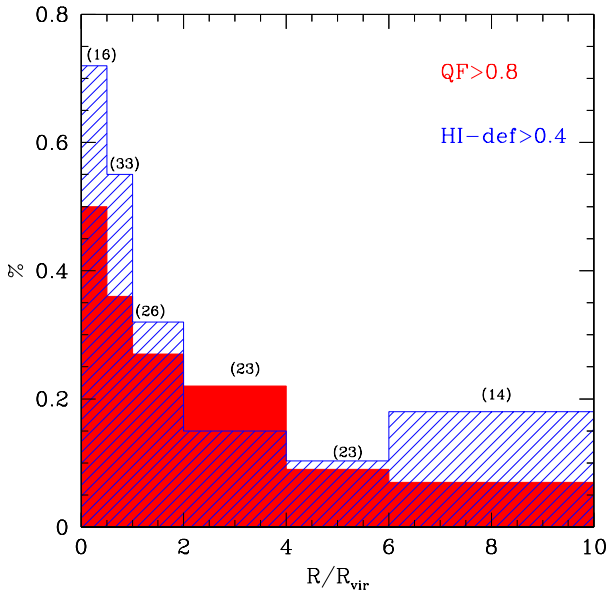

Fig. 18. Variation in the fraction of late-type galaxies with a quenching factor $QF > 0.8$ (red histogram) and an HI-deficiency $HI - def > 0.4$ (blue shaded histogram) and the distance from the centre of the Virgo cluster, in units of virial radii. The number galaxies for each bin of distance is given in parenthesis.

8.3. Rapid or slow environmental quenching?

We often read in the literature that the environmental quenching acts on long timescales (McGee et al. 2009; von der Linden et al. 2010; De Lucia et al. 2012; Taranu et al. 2014; Haines et al. 2015; Paccagnella et al. 2016). This apparent disagreement with our results comes from the fact that different definitions of quenching timescales are often used. In studies that are based on the combined analysis of statistical samples extracted from all-sky surveys such as the SDSS with the predictions of cosmological simulations or semi-analytical models, the quenching timescale is often defined as the time necessary to stop the

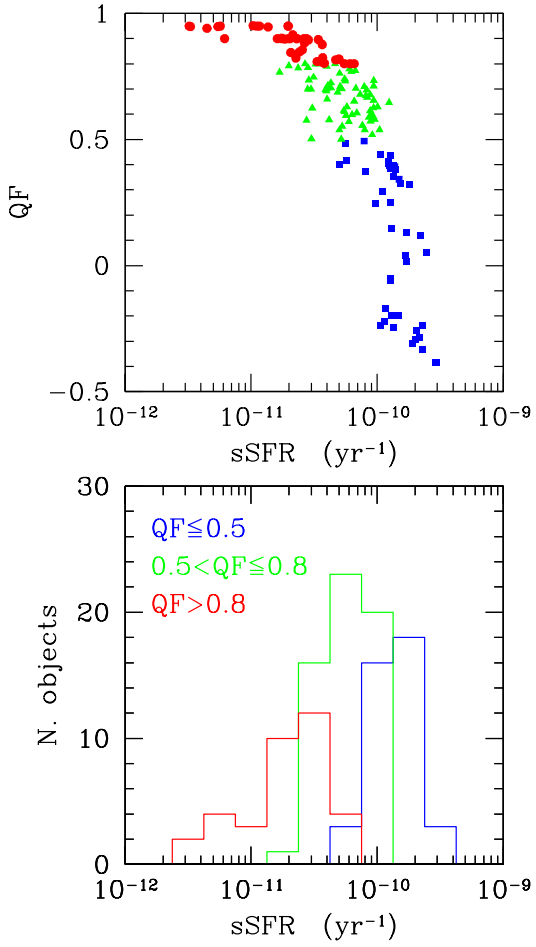

Fig. 19. *Upper panel*: relationship between the quenching factor QF and the specific star formation activity $sSFR$ for the late-type galaxies of the sample with a reduced $\chi^2_r \leq 3$. Blue filled squares, green triangles, and red circles are for galaxies where the derived quenching factor is $QF \leq 0.5$, $0.5 < QF \leq 0.8$, and $QF > 0.8$, respectively. *Lower panel*: $sSFR$ distribution for different quenching factors.

activity of star formation of a galaxy after it becomes a satellite of a larger system. Since the recent accretion of late-type galaxies in nearby clusters occurs principally through smaller groups (Gnedin 2003; McGee et al. 2009; De Lucia et al. 2010), this timescale is necessarily long even when the activity is quenched on short timescales only once the galaxy falls in the main cluster structure. The analysis of Wetzel et al. (2013) suggested a different evolution of the star formation activity of galaxies: first mildly declining on long timescales (2–4 Gyr), then with a rapid decrease (0.2–0.8 Gyr; "delayed-then-rapid"). The timescales that we estimate in this work, such as those derived for other Virgo cluster galaxies as described in Sect. 5.2, are rather representative of the timescale since the first stripping of the cold gas on the disc, which generally occurs when the galaxy is close to the pericenter along its orbit within the cluster. Recently, Oman & Hudson (2016) studied the quenching timescale and efficiency in massive clusters ($M_{\rm cluster} > 10^{13}\ M_\odot$) by comparing N-body simulations with the observed properties of SDSS galaxies. This work indicates that the quenching is 100% efficient ($QF = 1$) and occurs in the core of the cluster, at or near the first pericenter approach. These results convincingly indicate that ram pressure stripping is the main quenching mechanism in massive haloes. While their quenching timescale is the typical value for a population of galaxies in clusters, their results are in excellent agreement with our study of the histories of individual galaxies in Virgo.

It is also worth recalling that the dominant perturbing mechanism is expected to change as a function of the mass of the infalling galaxy and on quantities that strongly depend on the total dynamical mass of the cluster, such as the velocity dispersion of galaxies within the cluster, and the density and temperature of the intracluster gas. These quantities might also vary locally within the cluster since the distribution of the ICM is not uniform in terms of density and turbulence. Since all these parameters change also with redshift, we expect to have different results for different environments at different epochs, as is indeed observed (e.g. Balogh et al. 2016).

Another possible origin of the apparent disagreement between the short timescales derived in this work with those given in the literature might be the definition of quenched galaxies. Here we considered as quenched galaxies objects with an activity of star formation reduced by a factor of $QF > 0.5$ or $QF > 0.8$. These are still star-forming late-type galaxies. As depicted in Fig. 19, their typical specific star formation rate, defined as the current star formation rate divided by the total stellar mass given by the fit, ranges from a few 10^{-12} yr^{-1} to $sSFR \lesssim 10^{-10}$ yr^{-1}. A typical example is the massive NGC 4569 in the core of the Virgo cluster ($sSFR = 4.5 \times 10^{-11}$ yr^{-1}), characterised by a prominent Hα emission that is witness of an ongoing star formation activity. In SDSS-based works such as Wetzel et al. (2012, 2013), quenched galaxies are those with a specific star formation rate $sSFR \lesssim 10^{-11}$ yr^{-1}, a much more stringent definition than we used here. This difference is important in the framework of galaxy evolution. In a ram-pressure-stripping scenario, models and simulations indicate that most of the gas is stripped from the disc of spiral galaxies on short timescales ($\lesssim$0.2 Gyr) when the galaxy is at the pericenter along its orbit (Roediger & Henseler 2005; Roediger & Bruggen 2006, 2007; Tonnesen et al. 2007; Tonnesen & Bryan 2009). At this stage, however, there is still gas to sustain a moderate star formation activity on the inner disc of the perturbed galaxies (Boselli et al. 2006; Tonnesen & Bryan 2012; Bekki 2014; Roediger et al. 2015). Their quenching factor is therefore $QF < 1$ and their specific star formation activity $sSFR \gtrsim 10^{-11}$ yr^{-1}. The complete stripping of the gas, that is, the total quenching of the star formation activity ($QF = 1$), requires longer timescales (1–3 Gyr), consistent with what was found for the 22 early-type galaxies of the HRS. These timescales are fairly comparable to the timescale for the rapid quenching of the star formation activity of galaxies in rich environments found by Wetzel et al. (2012, 2013) and Oman & Hudson (2016) in the local Universe and by Muzzin et al. (2014) and Mok et al. (2014) at $z \sim 1$.

It seems therefore that the origin of most of the discrepancy between these works is in the definition of the quenching time, here defined as the epoch when galaxies drastically reduced ($\gtrsim$50%) their activity of star formation, in Wetzel et al. (2012, 2013) and in other works the time since a galaxy *first* became a satellite of a massive halo.

We conclude by mentioning that this analysis indicates that the quenching time can be accurately derived using our SED fitting technique only in 30% of the sample (galaxies with $QF > 0.8$), a value comparable to the number of HI-deficient objects ($HI - def > 0.4$; 33%) or of late-type galaxies located within one virial radius of Virgo (36%). Whenever the perturbing mechanism is milder than in Virgo, as it is probably the case in less massive haloes, we expect a less efficient quenching episode ($QF \ll 1$). For these galaxies it is hard to break all the degeneracies between star formation history,

IMF, metallicity, and dust attenuation, and thus derive accurate quenching timescales even using a UV-to-FIR SED fitting code as done in this work.

9. Conclusion

We studied the star formation history of the *Herschel* Reference Survey, a K-band-selected volume-limited complete sample of nearby galaxies using the CIGALE SED fitting code. The sample includes objects in the Virgo cluster and is therefore perfectly suited for understanding the role of the environment on galaxy evolution. To quantify the perturbation induced by the interaction with the hostile environment on the star formation activity of cluster galaxies, we adopted a truncated star formation history where the secular evolution is parametrised using the chemo-spectrophotometric physically justified models of Boissier & Prantzos (2000). To constrain any possible abrupt variation of the star formation activity of the Virgo cluster galaxies, we combined the UV to far-infrared photometric data (20 bands) with age-sensitive Balmer absorption line indices extracted from medium-resolution ($R \sim 1000$) integrated spectroscopy (3 bands) and Hα imaging data (1 band). Hα fluxes are necessary to constrain variations that occurred at very recent epochs ($\lesssim$100 Myr). The best fit to the data gives the quenching factor QF and the quenching age QA. The first parameter quantifies by how much the star formation activity has been reduced during the interaction ($QF = 0$ for unperturbed systems, $QF = 1$ when the star formation activity has been completely stopped), while QA gives the look-back time of the epoch of the quenching episode. We checked the reliability of the output parameters using mock catalogues of simulated galaxies and different star formation histories.

The analysis of the sample brought the following results:

(1) The quality of the SED fitting significantly increases when a truncated star formation history is used in all the HI-deficient galaxies of the sample, where the interaction with the hostile environment removed a large portion of the cold gas necessary to feed star formation.
(2) In these HI-deficient objects the activity of star formation is reduced by a factor of $50\% \leq QF < 80\%$ on timescales of $\simeq$135 Myr, and $QF \geq 80\%$ on timescales of $\simeq$250 Myr, and it is fully stopped after $\simeq$1.3 Gyr in early-type galaxies. These timescales are a factor of $\simeq$2 longer when a smoothly declining quenching process is assumed.
(3) The fraction of quenched late-type galaxies ($QF \geq 80\%$), as the fraction of HI-deficient objects, decreases by a factor of $\simeq$5 from the core of the Virgo cluster ($R/R_{\rm vir} \leq 0.5$) to the cluster periphery ($R/R_{\rm vir} \geq 4$).

The disagreement with the results obtained from the analysis of large samples such as the SDSS (e.g. Wetzel et al. 2012, 2013), which indicate longer timescales with a delayed-then-rapid quenching process, is only apparent since our timescales are representative of the rapid decrease of the star formation activity that occurred when galaxies enter the rich Virgo cluster, while those reported in the literature use the time since a galaxy became a satellite of a more massive halo. Furthermore, the timescales we used are those necessary to reduce the star formation activity by a factor of $\gtrsim$50−80%, while the timescales quoted in the literature lead to a full stop of the activity in the perturbed galaxies. All these results are consistent with a rapid quenching of the star formation activity of the late-type galaxies that were recently accreted on the Virgo cluster, as predicted by ram-pressure-stripping models. These results discard inefficient mechanisms such as starvation, which require very long ($\gtrsim$6 Gyr) timescales to significantly quench the star formation activity of the perturbed galaxies.

Acknowledgements. We thank the anonymous referee for constructive comments that improved the clarity of the manuscript. This research has been financed by the French national program PNCG. M. Fossati acknowledges the support of the Deutsche Forschungsgemeinschaft via Project ID 3871/1-1. L. Ciesla acknowledges funding from the European Union Seventh Framework Programme (FP7/2007-2013) under grant agreement No. 312725. This research has made use of the NASA/IPAC Extragalactic Database (NED) which is operated by the Jet Propulsion Laboratory, California Institute of Technology, under contract with the National Aeronautics and Space Administration.

References

Abramson, A., & Kenney, J. D. P. 2014, AJ, 147, 63
Abramson, A., Kenney, J. D. P., Crowl, H. H., et al. 2011, AJ, 141, 164
Baes, M., Clemens, M., Xilouris, E. M., et al. 2010, A&A, 518, L53
Bahé, Y. M., McCarthy, I. G., Balogh, M. L., & Font, A. S. 2013, MNRAS, 430, 3017
Balogh, M. L., Morris, S. L., Yee, H. K. C., Carlberg, R. G., & Ellingson, E. 1999, ApJ, 527, 54
Balogh, M. L., McGee, S. L., Mok, A., et al. 2016, MNRAS, 456, 4364
Bekki, K. 2009, MNRAS, 399, 2221
Bekki, K. 2014, MNRAS, 438, 444
Bekki, K., Couch, W. J., & Shioya, Y. 2002, ApJ, 577, 651
Bendo, G. J., Galliano, F., & Madden, S. C. 2012, MNRAS, 423, 197
Bigiel, F., Leroy, A., Walter, F., et al. 2008, AJ, 136, 2846
Böhringer, H., Briel, U. G., Schwarz, R. A., et al. 1994, Nature, 368, 828
Boissier, S., & Prantzos, N. 2000, MNRAS, 312, 398
Boissier, S., & Prantzos, N. 2001, MNRAS, 325, 321
Boissier, S., Boselli, A., Prantzos, N., & Gavazzi, G. 2001, MNRAS, 321, 733
Boissier, S., Prantzos, N., Boselli, A., & Gavazzi, G. 2003, MNRAS, 346, 1215
Boquien, M., Buat, V., Boselli, A., et al. 2012, A&A, 539, A145
Boquien, M., Boselli, A., Buat, V., et al. 2013, A&A, 554, A14
Boquien, M., Buat, V., & Perret, V. 2014, A&A, 571, A72
Boquien, M., Kennicutt, R., Calzetti, D., et al. 2016, A&A, 591, A6
Boselli, A. 2011, A Panchromatic View of Galaxies (Practical Approach Book) (Berlin: Wiley-VCH)
Boselli, A., & Gavazzi, G. 2006, PASP, 118, 517
Boselli, A., & Gavazzi, G. 2009, A&A, 508, 201
Boselli, A., & Gavazzi, G. 2014, A&ARv, 22, 74
Boselli, A., Gavazzi, G., Donas, J., & Scodeggio, M. 2001, AJ, 121, 753
Boselli, A., Boissier, S., Cortese, L., et al. 2005, ApJ, 623, L13
Boselli, A., Boissier, S., Cortese, L., et al. 2006, ApJ, 651, 811
Boselli, A., Boissier, S., Cortese, L., & Gavazzi, G. 2008, ApJ, 674, 742
Boselli, A., Boissier, S., Cortese, L., et al. 2009, ApJ, 706, 1527
Boselli, A., Eales, S., Cortese, L., et al. 2010a, PASP, 122, 261
Boselli, A., Ciesla, L., Buat, V., et al. 2010b, A&A, 518, L61
Boselli, A., Boissier, S., Heinis, S., et al. 2011, A&A, 528, A107
Boselli, A., Ciesla, L., Cortese, L., et al. 2012, A&A, 540, A54
Boselli, A., Hughes, T. M., Cortese, L., Gavazzi, G., & Buat, V. 2013, A&A, 550, A114
Boselli, A., Cortese, L., & Boquien, M. 2014a, A&A, 564, A65
Boselli, A., Cortese, L., Boquien, M., et al. 2014b, A&A, 564, A67
Boselli, A., Voyer, E., Boissier, S., et al. 2014c, A&A, 570, A69
Boselli, A., Cortese, L., Boquien, M., et al. 2014d, A&A, 564, A66
Boselli, A., Fossati, M., Gavazzi, G., et al. 2015, A&A, 579, A102
Boselli, A., Cuillandre, J. C., Fossati, M., et al. 2016, A&A, 587, A68
Brinchmann, J., Charlot, S., White, S. D. M., et al. 2004, MNRAS, 351, 1151
Bruzual, G., & Charlot, S. 2003, MNRAS, 344, 1000
Buat, V., Boissier, S., Burgarella, D., et al. 2008, A&A, 483, 107
Buat, V., Heinis, S., Boquien, M., et al. 2014, A&A, 561, A39
Byrd, G., & Valtonen, M. 1990, ApJ, 350, 89
Cayatte, V., van Gorkom, J. H., Balkowski, C., & Kotanyi, C. 1990, AJ, 100, 604
Cen, R., Pop, A. R., & Bahcall, N. A. 2014, Proc. Nat. Acad. Sci., 111, 7914
Chevallard, J., & Charlot, S. 2016, MNRAS, 462, 1415
Ciesla, L., Boselli, A., Smith, M. W. L., et al. 2012, A&A, 543, A161
Ciesla, L., Boquien, M., Boselli, A., et al. 2014, A&A, 565, A128

Ciesla, L., Boselli, A., Elbaz, D., et al. 2016, A&A, 585, A43
Colless, M., & Dunn, A. M. 1996, ApJ, 458, 435
Cortés, J. R., Kenney, J. D. P., & Hardy, E. 2015, ApJS, 216, 9
Cortese, L., Davies, J. I., Pohlen, M., et al. 2010, A&A, 518, L49
Cortese, L., Catinella, B., Boissier, S., Boselli, A., & Heinis, S. 2011, MNRAS, 415, 1797
Cortese, L., Ciesla, L., Boselli, A., et al. 2012a, A&A, 540, A52
Cortese, L., Boissier, S., Boselli, A., et al. 2012b, A&A, 544, A101
Cortese, L., Fritz, J., Bianchi, S., et al. 2014, MNRAS, 440, 942
Cortese, L., Bekki, K., Boselli, A., et al. 2016, MNRAS, 459, 3574
Cowie, L. L., & Songaila, A. 1977, Nature, 266, 501
Crowl, H. H., & Kenney, J. D. P. 2008, AJ, 136, 1623
da Cunha, E., Charlot, S., & Elbaz, D. 2008, MNRAS, 388, 1595
Davis, T. A., Alatalo, K., Bureau, M., et al. 2013, MNRAS, 429, 534
De Lucia, G., Poggianti, B. M., Aragón-Salamanca, A., et al. 2007, MNRAS, 374, 809
De Lucia, G., Poggianti, B. M., Halliday, C., et al. 2009, MNRAS, 400, 68
De Lucia, G., Weinmann, S., Poggianti, B. M., Aragón-Salamanca, A., & Zaritsky, D. 2012, MNRAS, 423, 1277
den Heijer, M., Oosterloo, T. A., Serra, P., et al. 2015, A&A, 581, A98
Draine, B. T., & Li, A. 2007, ApJ, 657, 810
Draine, B. T., Dale, D. A., Bendo, G., et al. 2007, ApJ, 663, 866
Dressler, A. 1980, ApJ, 236, 351
Dressler, A. 2004, in Clusters of Galaxies: Probes of Cosmological Structure and Galaxy Evolution (Cambridge University Press), 206
Dressler, A., Oemler, A., Jr., Couch, W. J., et al. 1997, ApJ, 490, 577
Dressler, A., Smail, I., Poggianti, B. M., et al. 1999, ApJS, 122, 51
Dressler, A., Oemler, A., Jr., Poggianti, B. M., et al. 2013, ApJ, 770, 62
Falcón-Barroso, J., Bacon, R., Bureau, M., et al. 2006, MNRAS, 369, 529
Font, A. S., Bower, R. G., McCarthy, I. G., et al. 2008, MNRAS, 389, 1619
Fontanot, F., De Lucia, G., Monaco, P., Somerville, R. S., & Santini, P. 2009, MNRAS, 397, 1776
Fossati, M., Gavazzi, G., Boselli, A., & Fumagalli, M. 2012, A&A, 544, A128
Fossati, M., Gavazzi, G., Savorgnan, G., et al. 2013, A&A, 553, A91
Fritz, J., Poggianti, B. M., Cava, A., et al. 2014, A&A, 566, A32
Fumagalli, M., Krumholz, M. R., Prochaska, J. X., Gavazzi, G., & Boselli, A. 2009, ApJ, 697, 1811
Gavazzi, G. 1987, ApJ, 320, 96
Gavazzi, G., Catinella, B., Carrasco, L., Boselli, A., & Contursi, A. 1998, AJ, 115, 1745
Gavazzi, G., Boselli, A., Mayer, L., et al. 2001, ApJ, 563, L23
Gavazzi, G., Boselli, A., Pedotti, P., Gallazzi, A., & Carrasco, L. 2002a, A&A, 396, 449
Gavazzi, G., Bonfanti, C., Sanvito, G., Boselli, A., & Scodeggio, M. 2002b, ApJ, 576, 135
Gavazzi, G., Zaccardo, A., Sanvito, G., Boselli, A., & Bonfanti, C. 2004, A&A, 417, 499
Gavazzi, G., Boselli, A., van Driel, W., & O'Neil, K. 2005, A&A, 429, 439
Gavazzi, G., O'Neil, K., Boselli, A., & van Driel, W. 2006a, A&A, 449, 929
Gavazzi, G., Boselli, A., Cortese, L., et al. 2006b, A&A, 446, 839
Gavazzi, G., Fumagalli, M., Cucciati, O., & Boselli, A. 2010, A&A, 517, A73
Gavazzi, G., Fumagalli, M., Fossati, M., et al. 2013a, A&A, 553, A89
Gavazzi, G., Savorgnan, G., Fossati, M., et al. 2013b, A&A, 553, A90
Gilbank, D. G., & Balogh, M. L. 2008, MNRAS, 385, L116
Gnedin, O. Y. 2003, ApJ, 589, 752
Gunn, J. E., & Gott, J. R., III 1972, ApJ, 176, 1
Guo, Q., White, S., Boylan-Kolchin, M., et al. 2011, MNRAS, 413, 101
Haines, C. P., Pereira, M. J., Smith, G. P., et al. 2015, ApJ, 806, 101
Haynes, M. P., & Giovanelli, R. 1984, AJ, 89, 758
Haynes, M. P., Giovanelli, R., & Chincarini, G. L. 1984, ARA&A, 22, 445
Henriques, B. M. B., White, S. D. M., Thomas, P. A., et al. 2015, MNRAS, 451, 2663
Hirschmann, M., De Lucia, G., Wilman, D., et al. 2014, MNRAS, 444, 2938
Jarrett, T. H., Chester, T., Cutri, R., Schneider, S. E., & Huchra, J. P. 2003, AJ, 125, 525
Kang, X., & van den Bosch, F. C. 2008, ApJ, 676, L101
Kauffmann, G., Heckman, T. M., White, S. D. M., et al. 2003, MNRAS, 341, 54
Kenney, J. D. P., van Gorkom, J. H., & Vollmer, B. 2004, AJ, 127, 3361
Kenney, J. D. P., Geha, M., Jáchym, P., et al. 2014, ApJ, 780, 119
Kennicutt, R. C., Jr. 1983, AJ, 88, 483
Kennicutt, R. C., Jr. 1998a, ApJ, 498, 541
Kennicutt, R. C., Jr. 1998b, ARA&A, 36, 189
Kennicutt, R. C., Jr., Armus, L., Bendo, G., et al. 2003, PASP, 115, 928
Kimm, T., Somerville, R. S., Yi, S. K., et al. 2009, MNRAS, 394, 1131
Kodama, T., Balogh, M. L., Smail, I., Bower, R. G., & Nakata, F. 2004, MNRAS, 354, 1103
Koopmann, R. A., & Kenney, J. D. P. 2004, ApJ, 613, 866
Larson, R. B., Tinsley, B. M., & Caldwell, C. N. 1980, ApJ, 237, 692
Levesque, E. M., Leitherer, C., Ekstrom, S., Meynet, G., & Schaerer, D. 2012, ApJ, 751, 67
López Fernández, R., Cid Fernandes, R., González Delgado, R. M., et al. 2016, MNRAS, 458, 184
Mastropietro, C., Moore, B., Mayer, L., et al. 2005, MNRAS, 364, 607
McGee, S. L., Balogh, M. L., Bower, R. G., Font, A. S., & McCarthy, I. G. 2009, MNRAS, 400, 937
McGee, S. L., Bower, R. G., & Balogh, M. L. 2014, MNRAS, 442, L105
McLaughlin, D. E. 1999, ApJ, 512, L9
Merritt, D. 1983, ApJ, 264, 24
Mok, A., Balogh, M. L., McGee, S. L., et al. 2013, MNRAS, 431, 1090
Moore, B., Lake, G., & Katz, N. 1998, ApJ, 495, 139
Moustakas, J., Kennicutt, R. C., Jr., Tremonti, C. A., et al. 2010, ApJS, 190, 233
Muñoz-Mateos, J. C., Gil de Paz, A., Boissier, S., et al. 2007, ApJ, 658, 1006
Muñoz-Mateos, J. C., Gil de Paz, A., Boissier, S., et al. 2009, ApJ, 701, 1965
Muñoz-Mateos, J. C., Boissier, S., Gil de Paz, A., et al. 2011, ApJ, 731, 10
Muzzin, A., Wilson, G., Yee, H. K. C., et al. 2012, ApJ, 746, 188
Muzzin, A., van der Burg, R. F. J., McGee, S. L., et al. 2014, ApJ, 796, 65
Newman, A. B., Ellis, R. S., Andreon, S., et al. 2014, ApJ, 788, 51
Noll, S., Burgarella, D., Giovannoli, E., et al. 2009, A&A, 507, 1793
Nulsen, P. E. J. 1982, MNRAS, 198, 1007
Nulsen, P. E. J., & Bohringer, H. 1995, MNRAS, 274, 1093
Oman, K. A., & Hudson, M. J. 2016, MNRAS, 463, 3083
Osterbrock, D. E., & Ferland, G. J. 2006, Astrophysics of gaseous nebulae and active galactic nuclei, 2nd edn. (Sausalito: University Science Books)
Paccagnella, A., Vulcani, B., Poggianti, B. M., et al. 2016, ApJ, 816, L25
Pacifici, C., Charlot, S., Blaizot, J., & Brinchmann, J. 2012, MNRAS, 421, 2002
Pacifici, C., da Cunha, E., Charlot, S., et al. 2015, MNRAS, 447, 786
Poggianti, B. M., & Barbaro, G. 1997, A&A, 325, 1025
Poggianti, B. M., Bridges, T. J., Carter, D., et al. 2001a, ApJ, 563, 118
Poggianti, B. M., Bridges, T. J., Mobasher, B., et al. 2001b, ApJ, 562, 689
Poggianti, B. M., Bridges, T. J., Komiyama, Y., et al. 2004, ApJ, 601, 197
Poggianti, B. M., Aragón-Salamanca, A., Zaritsky, D., et al. 2009, ApJ, 693, 112
Roediger, E., & Brüggen, M. 2006, MNRAS, 369, 567
Roediger, E., & Brüggen, M. 2007, MNRAS, 380, 1399
Roediger, E., & Hensler, G. 2005, A&A, 433, 875
Sandage, A. 1986, A&A, 161, 89
Sarazin, C. L. 1986, Rev. Mod. Phys., 58, 1
Sarzi, M., Falcón-Barroso, J., Davies, R. L., et al. 2006, MNRAS, 366, 1151
Schindler, S., Binggeli, B., & Böhringer, H. 1999, A&A, 343, 420
Schmidt, M. 1959, ApJ, 129, 243
Scott, T. C., Cortese, L., Brinks, E., et al. 2012, MNRAS, 419, L19
Silva, L., Granato, G. L., Bressan, A., & Danese, L. 1998, ApJ, 509, 103
Skrutskie, M. F., Cutri, R. M., Stiening, R., et al. 2006, AJ, 131, 1163
Smith, R. J., Marzke, R. O., Hornschemeier, A. E., et al. 2008, MNRAS, 386, L96
Smith, R. J., Lucey, J. R., Hudson, M. J., et al. 2009, MNRAS, 392, 1265
Smith, R. J., Lucey, J. R., Price, J., Hudson, M. J., & Phillipps, S. 2012, MNRAS, 419, 3167
Solanes, J. M., Manrique, A., García-Gómez, C., et al. 2001, ApJ, 548, 97
Stott, J. P., Smail, I., Edge, A. C., et al. 2007, ApJ, 661, 95
Stott, J. P., Pimbblet, K. A., Edge, A. C., Smith, G. P., & Wardlow, J. L. 2009, MNRAS, 394, 2098
Sun, M., Donahue, M., & Voit, G. M. 2007, ApJ, 671, 190
Taranu, D. S., Hudson, M. J., Balogh, M. L., et al. 2014, MNRAS, 440, 1934
Thomas, R., Le Fevre O., Scodeggio M., et al. 2016, A&A, submitted [arXiv:1602.01841]
Tonnesen, S., & Bryan, G. L. 2009, ApJ, 694, 789
Tonnesen, S., & Bryan, G. L. 2012, MNRAS, 422, 1609
Tonnesen, S., Bryan, G. L., & van Gorkom, J. H. 2007, ApJ, 671, 1434
Tran, K.-V. H., Franx, M., Illingworth, G. D., et al. 2007, ApJ, 661, 750
Tully, R. B., & Shaya, E. J. 1984, ApJ, 281, 31
Urban, O., Werner, N., Simionescu, A., Allen, S. W., & Böhringer, H. 2011, MNRAS, 414, 2101
Vollmer, B. 2003, A&A, 398, 525
Vollmer, B., & Huchtmeier, W. 2003, A&A, 406, 427
Vollmer, B., Cayatte, V., Boselli, A., Balkowski, C., & Duschl, W. J. 1999, A&A, 349, 411
Vollmer, B., Marcelin, M., Amram, P., et al. 2000, A&A, 364, 532
Vollmer, B., Cayatte, V., Balkowski, C., & Duschl, W. J. 2001, ApJ, 561, 708
Vollmer, B., Balkowski, C., Cayatte, V., van Driel, W., & Huchtmeier, W. 2004, A&A, 419, 35

Vollmer, B., Huchtmeier, W., & van Driel, W. 2005, A&A, 439, 921
Vollmer, B., Soida, M., Otmianowska-Mazur, K., et al. 2006, A&A, 453, 883
Vollmer, B., Soida, M., Chung, A., et al. 2008a, A&A, 483, 89
Vollmer, B., Braine, J., Pappalardo, C., & Hily-Blant, P. 2008b, A&A, 491, 455
Vollmer, B., Soida, M., Chung, A., et al. 2009, A&A, 496, 669
Vollmer, B., Soida, M., Braine, J., et al. 2012, A&A, 537, A143
von der Linden, A., Wild, V., Kauffmann, G., White, S. D. M., & Weinmann, S. 2010, MNRAS, 404, 1231
Vulcani, B., Poggianti, B. M., Fritz, J., et al. 2015, ApJ, 798, 52
Yagi, M., Yoshida, M., Komiyama, Y., et al. 2010, AJ, 140, 1814
Wang, L., Weinmann, S. M., & Neistein, E. 2012, MNRAS, 421, 3450
Weinmann, S. M., Lisker, T., Guo, Q., Meyer, H. T., & Janz, J. 2011, MNRAS, 416, 1197
Wetzel, A. R., Tinker, J. L., & Conroy, C. 2012, MNRAS, 424, 232
Wetzel, A. R., Tinker, J. L., Conroy, C., & van den Bosch, F. C. 2013, MNRAS, 432, 336
Wheeler, C., Phillips, J. I., Cooper, M. C., Boylan-Kolchin, M., & Bullock, J. S. 2014, MNRAS, 442, 1396
Whitmore, B. C., Gilmore, D. M., & Jones, C. 1993, ApJ, 407, 489
Wijesinghe, D. B., Hopkins, A. M., Brough, S., et al. 2012, MNRAS, 423, 3679
Wolf, C., Aragón-Salamanca, A., Balogh, M., et al. 2009, MNRAS, 393, 1302
Worthey, G. 1994, ApJS, 95, 107
Worthey, G., & Ottaviani, D. L. 1997, ApJS, 111, 377
Wu, P.-F., Gal, R. R., Lemaux, B. C., et al. 2014, ApJ, 792, 16

Appendix A: Exploring different star formation histories

To test the reliability of the output parameters of the SED fitting code, we also derived the quenching ages and quenching factors using two other star formation histories. In the first test, we used the same truncated star formation history as in Eq. (4), but left the rotational velocity of the galaxy as a free parameter and derived $QF(vel)$ and $QA(vel)$. In the second test we fixed the rotational velocity of the galaxies, but used a smoothly declining star formation history where the decrease of the activity is constant from the beginning of the interaction to the present epoch, as depicted in Fig. A.1 ($QF(SM)$ and $QA(SM)$):

$$SFR(t) = \begin{cases} SFR(t)_{\rm secular} & \text{if } t_0\text{–}t \geq QA \\ SFR(t_0 - QA)_{\rm secular} & \\ \quad \times[1 - QF + \frac{QF}{QA} \times (t_0 - t)] & \text{if } t_0\text{–}t < QA. \end{cases} \quad \text{(A.1)}$$

Figure A.2 shows the relationship between these newly derived parameters and the quenching ages and quenching factors derived in the paper assuming a fixed rotational velocity and the truncated star formation history given in Eq. (4).

Figure A.2 shows that the quenching factors derived using these three different assumptions on the star formation history and on the rotational velocity of the galaxies are very consistent provided that $QF \gtrsim 0.5$, that is, in the range of parameters analysed in this work. Figure A.2 also shows that the quenching ages derived using a truncated star formation history (Eq. (4)) are very consistent regardless of whether a fixed or a variable rotational velocity is used. This is even clearer whenever the quenching factor is large (the dispersion decreases from the blue to the green, the red, and the magenta symbols). Conversely, there is a systematic shift in the quenching ages when these parameters are derived assuming a truncated or a smoothly declining star formation history, the latter giving systematically higher values (the median values for the $QA(SM)/QA(T)$ are 2.58, 2.80, and 2.98 for the late-type galaxies with $0.5 < QF(T) \leq 0.8$, $QF(T) > 0.8$, and for the early-types, respectively). This is expected since the quenching ages derived using a smoothly declining star formation history should be considered as upper limits if the decrease of the activity is more rapid than the one predicted by Eq. (A.1).

Figure A.3 shows the distribution of the quenching ages derived using a truncated star formation history with the rotational velocity as a free parameter and a smoothly declining star formation history. It can be compared to Fig. 16, which was derived using a truncated star formation history with fixed rotational velocity. The median values derived for the three different prescriptions are given in Table A.1. The quenching ages derived using a truncated star formation history are very similar regardless the use of a fixed or a variable rotational velocity, with the exception of the early-type sample, where the QA is ≃a factor of 2 longer in the former case. The quenching ages derived using a smoothly declining star formation history are, as expected, a factor of ≃2 longer than those derived using a truncated star formation activity. The significantly larger number of filled symbols with respect to that of the empty ones in the lower panels of Fig. A.2, indicating galaxies with a ratio of the reduced χ^2_r derived from the SED fitting using a truncated-to-smoothly-declining star formation history is lower than unity ($\chi^2_r(T)/\chi^2_r(SM) < 1$), suggests

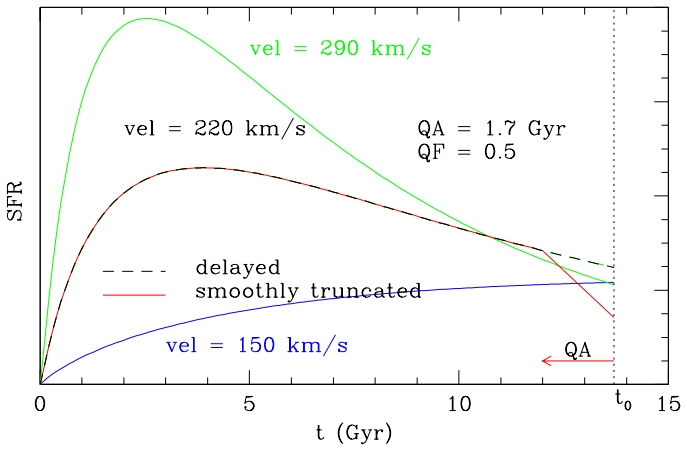

Fig. A.1. Parametric star formation history for a galaxy with a rotational velocity of 220 km s^{-1} (black dashed line), 290 km s^{-1} (green solid line), and 150 km s^{-1} (blue solid line). The black dashed line shows the delayed star formation history given in Eq. (1), the red solid line the smoothly declining history (Eq. (A.1)) for a galaxy with a rotational velocity of 220 km s^{-1}. This figure can be compared to Fig. 2.

Table A.1. Median quenching ages derived assuming different star formation histories for galaxies with $\chi^2_r \leq 3$.

Condition	$QA(T)$ Myr	$QA(vel)$ Myr	$QA(SM)$ Myr
Late-types, $0.5 < QF \leq 0.8$	136	127	302
Late-types, $QF > 0.8$	248	244	423
Early-types ($QF = 1$)	1319	614	2997

that the quality of the fit is higher when the truncated approximation is used (the number of free parameters in the two star formation histories are the same). This is also evident when Fig. A.3 is compared with Fig. 16, where only galaxies with a reduced $\chi^2_r \leq 3$ are plotted. More galaxies have a good-quality fit when a truncated vs. a smoothly declining star formation history is used. Another indication that a truncated star formation history is better suited to trace the evolution of the perturbed Virgo cluster galaxies than the smoothly declining history is gained from comparing Figs. 12 and A.4. The quenching ages derived using a truncated star formation history with a fixed rotational velocity better reproduce the estimates available in the literature and were derived using independent techniques for a dozen of galaxies in common (see Sect. 5). Although this small subsample of galaxies is probably biased because it is composed of systems expressly selected to have some evidence of an occurring ram-pressure-stripping event, we decided to adopt a truncated star formation history and a fixed rotational velocity as a reference case for the analysis done in this work. We recall, however, that the quenching ages given by the smoothly declining approximation, which in some cases gives better fits, can be taken as upper limits to the effective time taken by these galaxies to reduce their activity by a factor QF. The timescales to reduce the activity of late-type galaxies by a factor of $QF < 1$ are ≲500 Myr, and ≲3 Gyr (this approximately equals two crossing times of the Virgo cluster, Boselli & Gavazzi 2006) to stop the activity and transform late-type galaxies into lenticulars.

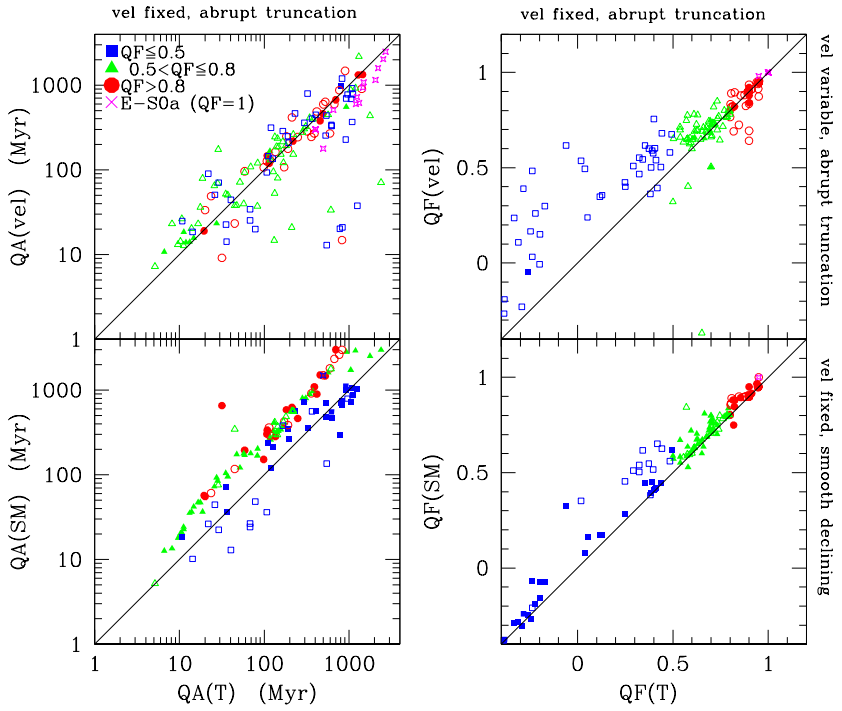

Fig. A.2. *Left panel*: relationship between the quenching age parameter derived using a truncated star formation history (Eq. (4)) with the rotational velocity as a free parameter ($QA(vel)$, *upper panel*) or using a smoothly declining star formation history (Eq. (A.1)) with fixed rotational velocity ($QA(SM)$, *lower panel*) vs. the one derived using a truncated star formation history (Eq. (4)) determined using a fixed value for the rotational velocity $QA(T)$. Filled symbols and crosses indicate galaxies where the reduced χ^2_r in the truncated model with fixed velocity is smaller than the one derived with the smoothly declining star formation history or the truncated one with the rotational velocity as a free parameter, empty symbols for $\chi^2_r(T)/\chi^2_r(SM, vel) > 1$. Blue squares, green triangles, and red circles are for late-type galaxies with a quenching factor $QF \leq 0.5$, $0.5 < QF \leq 0.8$, and $QF > 0.8$, respectively, and the magenta crosses and empty stars show early-type galaxies. The black solid line shows the 1:1 relation. Only galaxies with a $\chi^2_r \leq 3$ are plotted. *Right panel*: same relationships for the quenching factor.

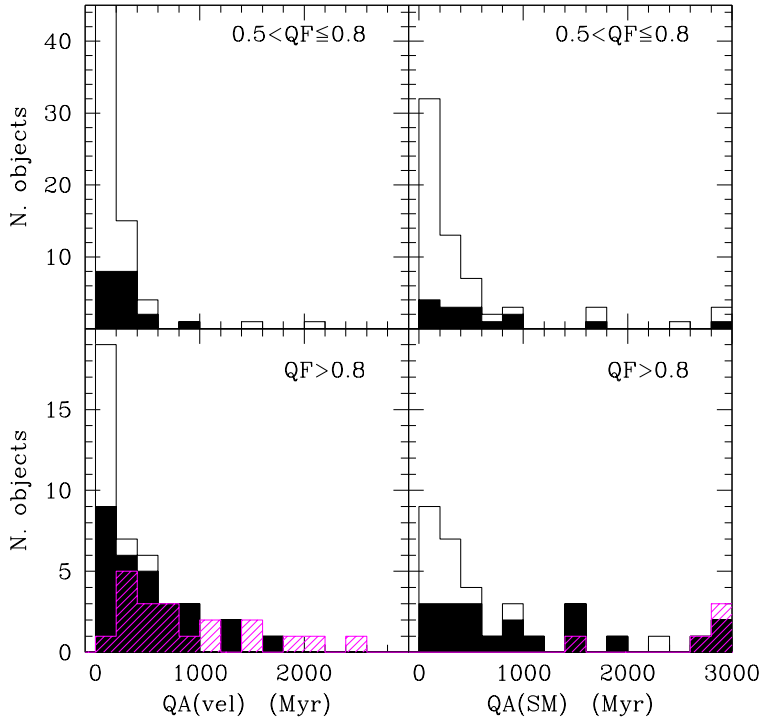

Fig. A.3. *Left panels*: distribution of the quenching age parameter $QA(vel)$ for galaxies with $\chi^2_r \leq 3$ and a quenching factor $0.5 < QF(vel) \leq 0.8$ (*upper panel*) and $QF(vel) > 0.8$ (*lower panel*) derived using a truncated star formation history (Eq. (4)) with the rotational velocity as a free parameter. The magenta histogram shows early-type galaxies, the empty histogram all late-type galaxies, and the black shaded histogram the HI-deficient ($HI - def > 0.4$) late-type systems. *Right panels*: the same distributions derived using a smoothly declining star formation history (Eq. A.1) and a fixed rotational velocity.

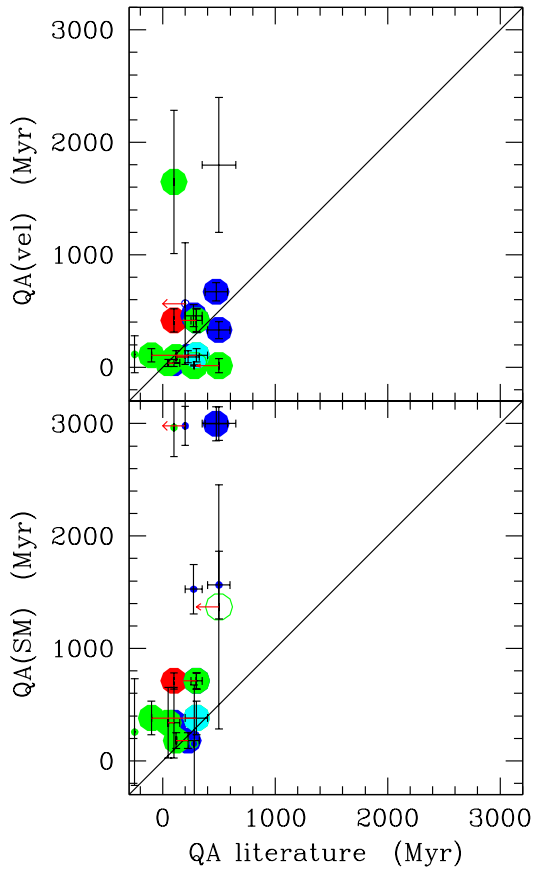

Fig. A.4. Relationship between the quenching age derived using our SED fitting technique and that derived using multizone chemo-spectrophotometric models of galaxy evolution for NGC 4569 (red dot), dynamical models based on the HI and CO gas kinematics (green dots), IFU spectroscopy of the outer disc of some cluster galaxies (blue dots), and photometric data compared to population synthesis models (cyan dots) (see Fig. 12 for comparison). In the upper panel the model SEDs are derived using a truncated star formation history (Eq. (4)) and leaving the rotational velocity as a free parameter, in the lower panel the rotational velocity is fixed and the star formation history is smoothly declining (Eq. (A.1)). Filled symbols are used for galaxies with a quenching factor $QF > 0.5$, empty dots for those with $QF \leq 0.5$. Large symbols are for galaxies with a reduced $\chi^2_r \leq 3$, small symbols for $\chi^2_r > 3$. The red lines connecting two points are used to indicate galaxies for which two independent quenching ages are available in the literature. The red arrows indicate upper limits to the quenching age given in the literature. The solid diagonal line indicates the 1:1 relationship.